# Coherent GNSS-Reflections Characterization Over Ocean and Sea Ice Based on Spire Global CubeSat Data

Carolyn J. Roesler, Y. Jade Morton, *Fellow, IEEE*, Yang Wang, *Student Member, IEEE*, and R. Steven Nerem

***Abstract*— This article assesses the coherency of Global Navigation Satellite System (GNSS) signals reflected off the oceans and sea ice under grazing angle geometries and received aboard low Earth orbit (LEO) CubeSats for precision altimetry applications. The coherency is characterized as a function of ocean surface conditions and reflected signal parameters based on Spire Global CubeSat data collected from January to April 2019. The data contain 50-Hz GPS L1 and L2 carrier phase estimations obtained by open-loop tracking. Indicators based on the circular statistics of the excess-phase noise are developed to identify coherent and semicoherent reflections. Based on these indicators, we found that ∼1% and 44% of GPS reflections over the ocean and sea ice, respectively, have potential for precision altimetry. The coherent and semicoherent reflection rates reach 23% in areas less than 200 km from the coastline and under calm sea conditions. Over young sea ice over the Arctic, this rate can be as high as 70%. There is a strong relationship between coherency and signal strength, and the coherency occurrence rate improves as the grazing angle decreases. The quality of the L1 and L2 coherent reflections is similar over sea ice, while, for reflections over the ocean, L1 signals are predominantly noisier and less coherent than the L2 signals. Using a postprocessing filtering method, the semicoherent reflections can achieve a similar level of altimetry precision as that of the coherent ones, thereby increasing the along-track length of the retrieved altimetry profile.**

***Index Terms*— Carrier phase estimations, coherent reflections, GPS reflection, ocean surface, precision altimetry, sea ice, semicoherent reflections.**

## I. Introduction

THE current global gridded sea surface topography maps are provided by satellite radar altimeters, such as Jason-3 and Sentinel 3A [1]. These maps cannot resolve features with a spatial scale of less than ∼100 km, and their revisit time is ∼10 days. To improve ocean and climate modeling, better spatial and temporal resolutions of mesoscale sea surface height (SSH) observations are needed [2]. The upcoming Surface Water and Ocean Topography (SWOT) satellite mission is expected to offer a 2-D spatial resolution of 10 km × 10 km along its swath although its performance at the mesoscale and submesoscale remains to be demonstrated [3].

A potential alternative to improve the SSH sampling is to operate a constellation of low-cost CubeSats on low Earth orbits (LEOs) that collect the Global Navigation Satellite System (GNSS) signals reflected off the ocean surface. It relies on the bistatic GNSS Reflectometry (GNSS-R) technique applied to space-based platforms, first suggested by Martin-Neira [4] in 1993. Remote sensing using signals of opportunity, such as GNSS reflected off the ocean surface, has found applications including ocean winds [5], significant wave height (SWH) [6], sea roughness [7], and ocean altimetry [8]–[10]. Several GNSS-R missions have been deployed in recent years. For example, the delay Doppler maps (DDMs) produced from the U.K. TechDemoSat-1 (TDS-1) and NASA's Cyclone GNSS (CYGNSS) demonstrated the feasibility of the GNSS-R for ocean altimetry even though the receiver systems were optimized for ocean wind [8], [11]. The DDMs represent the power of the reflected GNSS signal as a function of code delay and Doppler frequency via cross correlation with a locally generated reference signal. Since they are based on the chip length of the GNSS ranging code, they produce along-track SSH at meter-level precision and tens of km footprint size that is inadequate for mesoscale oceanography (e.g., [8] and [12]). However, the first evidence of mesoscale ocean eddies signature has been detected by combining the dense spatial and temporal data coverage of the CYGNSS constellation [13].

To improve the altimetric precision, GNSS-R carrier phase observables are used. If the GNSS reflections have sufficient coherent energy, then the carrier phase can be estimated with cm-level precision at ∼1-3 km spatial resolution at low grazing angles. This enables the application to surfaces that are smooth relative to the GPS L-band wavelength (∼20 cm). Low grazing angles over sea ice or relatively calm ocean surfaces help to reduce the surface roughness effect on the carrier signal. At the extreme near tangent to the surface angles, spaceborne interferometric carrier phase beats between direct and sea ice reflected signals were initially observed during a CHAMP occultation [14], but these near zero-grazing angles are too low for precision altimetry. Experiments on coherent reflection tracking for altimetry have been conducted on ground-based GNSS receivers [15]–[19]

Manuscript received May 3, 2021; revised August 24, 2021 and October 20, 2021; accepted November 11, 2021. Date of publication November 23, 2021; date of current version February 17, 2022. This work was supported by the National Aeronautics and Space Administration (NASA) under Grant 80NSSC20K1082 and Grant 80NSSC20K1738. *(Corresponding author: Carolyn J. Roesler.)*

The authors are with the Ann and H. J. Smead Department of Aerospace Engineering Sciences, University of Colorado Boulder, Boulder, CO 80303 USA (e-mail: carolyn.roesler@colorado.edu; jade.morton@colorado.edu; yang.wang-2@colorado.edu; nerem@colorado.edu).

Digital Object Identifier 10.1109/TGRS.2021.3129999

and airborne receivers [20], [21], including stratospheric balloons [22]. The design of coherent GNSS-R from a CubeSat was first proposed in [23]. Simulation studies were conducted to formulate the prerequisites and retrieval expectations of spaceborne ocean phase altimetry [24]. Recently, processing of raw intermediate frequency (IF) GNSS-R signal recorded on TDS-1 and the CYGNSS satellites demonstrated that carrier phase altimetry from space can achieve better than 10-cm precision over sea ice [25], lakes [10], [26], a river [27], calm oceans [9], [10], and rain forest [10].

Experiments with airborne receivers found that reflection signal grazing elevation angles within 5°–30° and over surfaces with low wind speeds are more likely to provide coherent GNSS ocean reflections [20]. The first analysis of CYGNSS carrier-phase altimetry data over the oceans around Central America confirms that under grazing geometries coherency occurs for wind speeds <6 m/s and wave heights less than 1.6 m [9]. Spaceborne studies show that sea ice has the potential for strong GNSS coherent reflections [14], [25], [28], [29]. However, not enough real data have been collected to determine if the phase-delay altimeter technique from space is viable over a wide range of ocean conditions.

Since 2019, Spire Global Inc. has been operating several polar-orbiting GNSS radio occultation (RO) CubeSats in GNSS-R mode for ocean altimetry by updating their onboard receiver software. These CubeSats already provide atmospheric profiles that are incorporated into weather forecasting models [30]. The new altimetry mode tracks the GPS L1 and L2 signal carrier phases reflected off the ocean surface at grazing angles. Initial results show that the data capture coherent reflections over sea ice and ocean [29], [31], [32] with altimetry retrievals at cm level over sea ice and ∼2-cm RMS relative to a mean sea surface (MSS) over the ocean [33].

This article assesses the quality of phase-delay altimetry data collected by four Spire CubeSats from January to April 2019. Two characteristics of the Spire CubeSats differ from TDS-1 and CYGNSS. First, unlike the CYGNSS and TDS-1 that use nadir pointing antennas to receive the reflection signals, the Spire CubeSat side-looking RO antennas are repurposed for collecting reflection data at grazing angles. The antenna gain is low for signals with elevations above the Brewster angle because the signals are predominately left-hand circular polarization (LHCP) [34]. The Brewster angle is about 30°, 18°, and 7° for first-year/multiyear (MY) sea ice, new/young sea ice, and sea water, respectively, at GPS L-band frequencies [35], [36]. Second, the Spire CubeSats track both L1 and L2 frequencies, which should improve the ionospheric correction. However, the hardware biases in the current Spire CubeSats receivers are not accurately calibrated, which impacts the absolute ionospheric correction.

Once the high-rate carrier phase data are gathered, a coherency detection scheme is required to separate signals with precise range information from random noise. The detectability of coherent phase measurements depends on the receiver platform and hardware, carrier phase tracking software, reflection surface properties, and the incident angle of the GNSS signal at the specular point (SP). For signals reflected over smooth ocean surfaces, we expect the coherently reflected signal phase to last over a reasonable amount of time. Techniques to separate the coherent and noncoherent parts of the reflection signal waveform based on coherent and noncoherent averaging have been tested on the ground, airborne, and space-based platforms (e.g., [22], [37], and [38]). For example, Semmling *et al.* [16] applied a maximum phase gradient algorithm to obtain the continuous coherent phase observations for data obtained from a ground-based GNSS interferometric receiver over Disco Bay. For the same experimental setting, Liu *et al.* [18] implement an algorithm based on the circular nature of the carrier phase to improve the tracking performance over rough-sea states.

For spaceborne observations, the reflection geometry and the speed of the receiver platform are different from the ground-based systems. There are several ongoing investigations for ways to detect coherently reflected GPS signals in CYGNSS data. For example, the phase power method argues that, if the phases are coherent, the signal power will systematically increase with the integration time relative to a nominal power, while this is not true for noncoherent reflections characterized with random phases [39]. The Entropy method is based on the assessment of the principal axis decomposition of the zero-delay Doppler waveform: if there is mainly one principal axis of energy direction, the signal is coherent [40]. The third method analyzes the extent of power spread in the delay Doppler space from the CYGNSS level 1 DDM data product: the wider the power spread, the less coherent are the reflections [41]. These methods are all based on indicators derived from reflected signal power. Analysis indicates that they offer similar coherent detection results over homogeneous land surfaces [42].

Not all these detection schemes can be applied to the Spire 50-Hz phase-delay observations due to the lack of access to the power waveform from the correlator's output. Moreover, signal power alone may not be a reliable indicator of the usability or quality of the carrier phase measurements. Our examination of three-month Spire GNSS-R data indicates that a high signal power does not always correspond to high-quality carrier phase estimations (see discussions in Section IV). Alternative approaches that directly utilize carrier phase measurements must be explored for reliable coherent detection schemes. Roesler *et al.* [29] presented a GNSS-R signal coherency test based on the circular nature of the excess-phase measurements. Wang *et al.* [32] proposed a support vector machine (SVM)-based machine learning method that utilizes the circular statistics-based coherency test as its feature and demonstrated 98% detection accuracy when applied to the Spire data. In this article, we introduce two additional coherency detectors based on the carrier phase circular statistics: one derived from the excess-phase rate and the other from phase noise. These detectors not only detect coherent signals but can also be used to identify semicoherent reflections. The semicoherent reflections can be further processed to yield a precision phase range for altimetry applications. The introduction of the semicoherent reflections allows us to extend the altimetry measurement intervals.

The remainder of this article is organized as follows. Section II describes the Spire CubeSat data used in this study.

Section III focuses on the methodologies of carrier phase estimation, the coherency detectors extraction, the detector's sensitivity analysis, and the classification of coherency regimes. Section IV presents the results of applying the coherency detection and classification to GPS L1 and L2 reflection data collected by Spire CubeSats from January to April 2019. A comparison of the results with the signal-to-noise ratio (SNR)-based indicator is presented. The detected coherent and semicoherent signal levels as functions of sea surface conditions, spatial patterns, satellite elevation angle, received signal SNR, and dependence on wind speed, wave height, and ice age, as well as the quality of the L1 and L2 reflection signals, are discussed in this section. Section V provides examples of altimetry retrievals to validate the performance of the indicators. Conclusions are drawn in Section VI.

## II. Spire Global GNSS-R Data

Spire Global Inc. started building commercial GNSS RO CubeSats in 2016. By July 2019, it had about 25+ operational commercial CubeSats orbiting at ∼500-km altitude in various inclinations performing GPS-RO measurements over the ocean and poles. The Lemur-2 microsatellites are equipped with a dual-frequency (L1 and L2) zenith antenna for precise orbit determination (POD) and high-gain forward- or backward-looking antennas to collect dual-frequency RO data. They carry the proprietary STRATOS payload. The STRATOS receiver outputs are used to retrieve atmospheric profiles and ionospheric measurements. For more information on Spire CubeSat capabilities, readers are referred to [43].

Starting in 2019, Spire reprogrammed some of their operational STRATOS receiver software onboard the CubeSats to operate in a phase-delay altimetry mode. The CubeSats collect the direct and reflected signals using the same side-looking RHCP antenna, which was originally intended for RO measurements. Only incident GPS reflection signals at low grazing angles between 5° and 30° over the ocean surface and lasting between 1 and 5 min are collected. The onboard software performs open-loop (OL) tracking of the direct and reflected GPS L1 and L2 carrier signals to generate 50-Hz carrier phase estimations [44].

We evaluate observations collected between January and April 2019 from four Spire LEO CubeSats (SVN 084, 086, 088, 090) with a total of 2500 reflection events. Fig. 1 shows the SP tracks of these reflection events, color-coded according to the reflection signal SNR values. Table I lists the date and number of events for each Spire CubeSat. The variations in the collection dates and number of events are due to the fact that not all four Spire CubeSats are in the GNSS-R altimetry mode during the same time period. The number of daily events collected may not represent the full capacity of a functional altimetry mode. Note that SVN 084 has a lower inclination orbit than the others and captures reflections up to a maximum latitude of 60°, while all others also cover the poles. To separate reflections between the ocean and sea ice, we construct a sea-ice flag based on the weekly National Snow and Ice Data Center (NSIDC) sea-ice extent product [45].

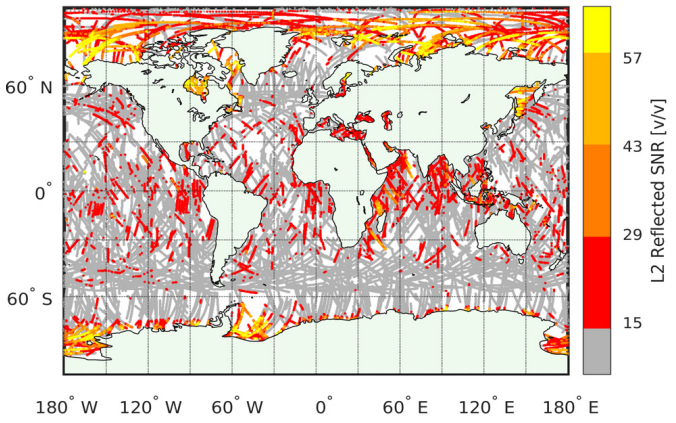


Fig. 1. Spire Global CubeSat GNSS-R data coverage map. The tracks of reflections SPs are color-coded according to the received GPS L2 signal SNR averaged over 1 s. Reproduced from [29, Fig. 2].

TABLE I
Spire SVNs' Date Span and Number of Reflection Events During January to April 2019

| Spire SVN | 084 | 086 | 088 | 090 |
|---|---|---|---|---|
| Dates (2019) | 3/21-4/18 | 1/8-1/26 | 3/15-4/18 | 1/24-2/10 |
| # of events | 998 | 276 | 738 | 484 |

## III. Methodologies

### A. GNSS-R Carrier Phase Estimation Method

The OL carrier phase tracking algorithm employed by the Spire CubeSats generates a local carrier signal replica based on *a priori* phase model $\phi_0$. The residual carrier phase $\delta\phi$ is the difference between that of the received signal $\phi$ and the local replica $\phi_0$. Both $\delta\phi$ and SNR are estimated from the in-phase ($I$) and quadratic phase ($Q$) components of the prompt correlators at a 50-Hz sampling rate

$$\delta\phi_L = \arctan(Q_L/I_L) \tag{1}$$

$$\text{SNR}_L = a_L\sqrt{I_L^2 + Q_L^2} \tag{2}$$

where the subscripts $L = 1, 2$ indicate GPS L1 and L2 carriers, respectively, $a_1 = 0.1263$, and $a_2 = 0.0736$ [44].

The residual phase and the *a priori* phase model are used to obtain phase estimation

$$\phi_L(t) = \phi_{L0}(t) + \delta\phi_L(t) + 2n\pi \tag{3}$$

where $n$ is an integer carrier cycle ambiguity constant along each SP track (event). The onboard *a priori* phase model $\phi_{L0}$ estimates the SP on the WGS84 reference ellipsoid based on the locations of the GPS satellite and the CubeSat following geometric optics reflection laws. The SP footprint of the carrier phase estimations is represented by the first Fresnel zone (FFZ), and for a flat surface, its size increases as the SP satellite elevation decreases [24], [46]. For a CubeSat at an altitude of ∼500 km, the instantaneous footprint is an ellipse with a major axis extent ∼1.4–5 km in the along-track direction and a relatively constant minor axis extent ∼1 km. For the Spire events collected in an RO setting with a horizon-looking antenna, the SP ground speed decreases with satellite

TABLE II

FFZ DEPENDENCE ON SATELLITE ELEVATION FOR A CUBESAT ORBIT HEIGHT OF 500 KM AND MEDIAN GROUND SCAN SPEED FOR A HORIZONTAL-LOOKING RO ANTENNA. THE CURVATURE OF THE EARTH HAS BEEN TAKEN INTO ACCOUNT

| Elevation (°) | 5 | 10 | 15 | 20 | 25 | 30 |
|---|---|---|---|---|---|---|
| Semi-major axis (km) | 2.5 | 1.9 | 1.4 | 1 | 0.8 | 0.7 |
| Semi-minor axis (km) | 0.67 | 0.58 | 0.53 | 0.5 | 0.45 | 0.43 |
| Ground speed (km/s) | 4 | 4.4 | 4.8 | 5.2 | 5.5 | 5.7 |

elevation, and the steepness of the change depends on the geometry evolution. Table II lists footprint size and typical ground scan speed for a range of elevations. The phase coherency indicators presented in this article use 1-s 50-Hz phase measurements. The along-track resolution of the indicators is ∼6–8 km for signal elevation between 5° and 30°. We should note that there are other factors besides the FFZ that influence coherency and altimetry retrieval precision. For example, the RHCP reflectivity increases as the elevation decreases below the Brewster angle; the amplitude of the RHCP reflected signals is larger below the Brewster angle, which includes both coherent and incoherent terms. Another point is a higher coherent-to-incoherent scattering ratio at grazing angles according to the Rayleigh criterion. These factors improve the carrier phase observation quality at low elevations. However, troposphere model corrections have larger errors for very low grazing angle measurements that negatively impact the precision of altimetry retrieval.

### *B. GNSS-R Carrier Phase Coherency Indicators*

Determination of the level of coherence in the reflected carrier phase time series is the prerequisite to the utilization of the carrier phase estimations for precision altimetry applications. Fig. 2 illustrates the difference between coherent and noncoherent reflected signals. Fig. 2(a) shows two 2-s segments of reflected GPS PRN 24 L2 carrier phase estimations collected on February 1, 2019, by the Spire SVN 090 CubeSat. The coherent nature of the phase measurement is apparent in the top left plot as indicated by the continuous phase values with a relatively constant phase rate, while the top right plot shows random phase values that are characteristics of noncoherent signals. If the phase is coherent, then we should be able to express the phase variation as a rotating phasor in time. For the noncoherent signal, its corresponding phasor is a bundle of random points. These are indeed the cases, as shown in Fig. 2(b). The coherency detectors described below are derived from the phasor representation of the phase measurements.

Before we dive into the specific coherency detectors, it is important to address the phase measurement model. The reflection signal excess phase is the difference between the received and modeled phases $\phi_{L0}$. It is computed in real time by the GNSS receiver onboard a CubeSat. The reflected signal phase model $\phi_{L0}$ is based on the geometric range between the GPS satellite, the SP computed on the WGS84 ellipsoid, and the Spire CubeSat antenna. The reflection signal excess phase includes unmodeled errors in the GPS satellite and the CubeSat positions, instrument and clock bias, atmospheric and

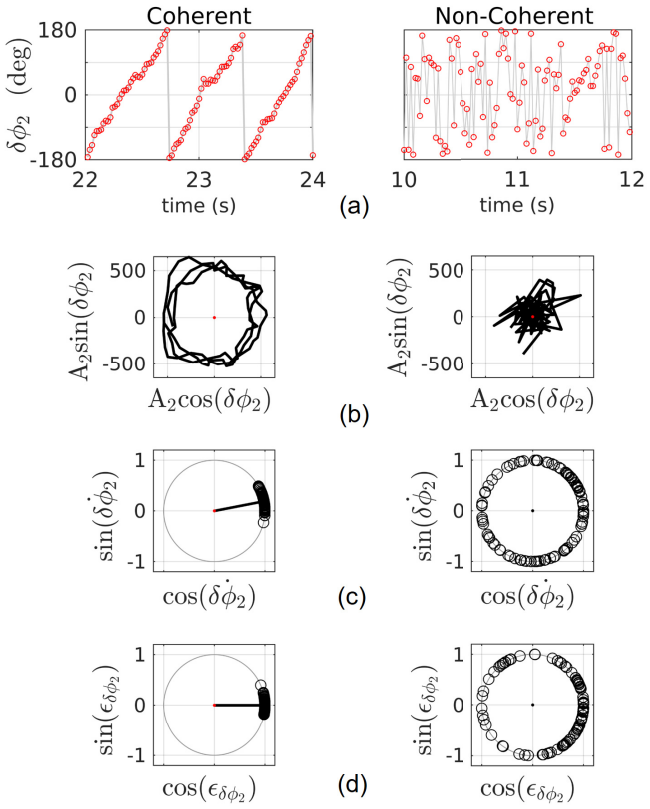


Fig. 2. GPS PRN 24 L2 reflection signal carrier excess phase $\delta\phi_2$ obtained from Spire CubeSats SVN 090 on February 1, 2019. The signal was transmitted from GPS PRN 24 and received by Spire SVN 090 starting at 02:26:37 UTC. The plots on (left) are an example of the coherent dataset from 22 s to 24 s, while the plots on (right) are an example of the noncoherent dataset from 10 to 12 s. (a) Excess-phase time series. (b) Polar representations of the excess phase. (c) Polar representations of the angular phase rate. (d) Polar representations of the angular phase noise.

ionospheric effects, and an error due to the unknown height of the reflection surface. At grazing incident angles and for receivers onboard the CubeSats, the spatial scale variations of the atmospheric and ionospheric effects are much larger than that of the sea surface variations along the ∼4-km ground track covered over 1 s. Therefore, the excess phase delay variations are mainly driven by the unmodeled changes in the signal propagation geometric path. The reflection surface height above the ellipsoid over the coherent footprint typically varies slowly along this ∼4-km ground track over the ocean and sea ice. Consequently, when the phase is coherent, its phase rate is expected to change continuously and gradually.

Since the time interval between two adjacent measurements is constant, the phase rate is directly dependent on the angular phase increment between two adjacent measurements $\delta\dot{\phi}_L = \delta\phi_L(i+1) - \delta\phi_L(i)$. If the phase rate is relatively constant, then, in a polar coordinate, $\delta\dot{\phi}_L$ samples should cluster along a narrowly focused direction. When the phase is completely noncoherent, the $\delta\dot{\phi}_L$ samples are uniformly distributed around the unit circle. Fig. 2c) shows $\delta\dot{\phi}_L$ samples in the polar coordinates for the coherent and noncoherent segments of data. The clear distinctions between the phase rates in the polar representation for these two examples indicate that it may serve as an indicator for signal coherency.

The circular statistics derived from the phase rate in the polar representation have been applied to ground-based GNSS-R altimetry to detect coherent segments [18] and estimate the sea surface height [47]. We apply the same concept to the space-based GNSS-R measurements. Roesler *et al.* [29] used two parameters, the circular length, and the circular kurtosis to determine whether an angular set $a_i, i = 1, 2, \ldots, N$ is uniformly distributed around the unit circle. The definitions for the two parameters are based on [48].

1) *Circular Length:* It is defined as the length of average of the unit vectors of the dataset

$$\zeta = \frac{1}{N}\left|\sum_{i=1}^{N}\cos a_i + \sum_{i=1}^{N}\sin a_i\right|. \tag{4}$$

2) *Circular Kurtosis:* A measure of the "peakedness" of an angular dataset

$$K = \frac{1}{N}\sum_{i=1}^{N}\cos(2(a_i - \bar{a}_i)) \tag{5}$$

where $\bar{a}_i$ is the mean of the dataset. If $a_i$ is uniformly distributed over the unit circle, then $\zeta = 0$ and $K <= 0$. If the dataset is completely coherent, the phasors should be aligned in one direction, and $\zeta = 1$ and $K = 1$. The closer the $\zeta$ and $K$ values are to 1, the more coherent the signal is. The phase rate circular length and circular kurtosis are the indicators used in [29].

In this article, we introduce the circular statistics for phase noise $\epsilon_{\delta\phi}$ and compare its performance with that of the phase rate $\delta\dot{\phi}_L$. The phase noise $\epsilon_{\delta\phi}$ is computed by subtracting a smoothed version of the excess phase. The phase noise $\epsilon_{\delta\phi}$ for the same two segments of data shown in Fig. 2(a) is plotted in the polar coordinate in Fig. 2(d). For completely noncoherently reflected signals, $\epsilon_{\delta\phi}$ behaves like noise. For coherent reflections, $\epsilon_{\delta\phi}$ varies smoothly and contains information about the reflection surface properties. Cai *et al.* [49] show that the additive noise on the phase delay of a GNSS signal follows a Von Mises distribution, which is also referred to as the circular normal distribution. Higher noise power is associated with a wider distribution peak. For the examples given in Fig. 2, the polar plots for the phase rate $\delta\dot{\phi}_L$ and phase noise $\epsilon_{\delta\phi}$ are similar for the noncoherent phase. When the phase is coherent, the mean phase noise direction is near zero, as shown in Fig. 2(d). In Section II-C, we show that the phase-noise statistics are more sensitive to the phase-rate variations within the 1-s period and are a better indicator of coherency than that of the phase rate.

### C. Phase Coherency Indicators Sensitivity Analysis

We use a 2-s excess phase $\delta\phi$ data segment collected by a Spire CubeSat to analyze the sensitivity of the phase rate and phase noise circular statistics to the coherency level. The first 1-s data are coherent, while the remaining 1 s is noncoherent, as shown in Fig. 3. From these 2-s data, we created 11 sets of 1-s data segments by sliding a 1-s window from left to right, as illustrated in Fig. 3. These 1-s data segments progressively evolve from being completely coherent in Set 1 to completely noncoherent in Set 11. We then add random noise from a circular Von Mises distribution to each data segment, with noise levels ranging from 0° to 180°. Each noise level is simulated 1000 times to produce a statistical performance measure. At each noise level, the circular length and kurtosis are computed for the phase noise $\epsilon_{\delta\phi}$ and the phase rate $\delta\dot{\phi}_L$, for each of the 11 sets.

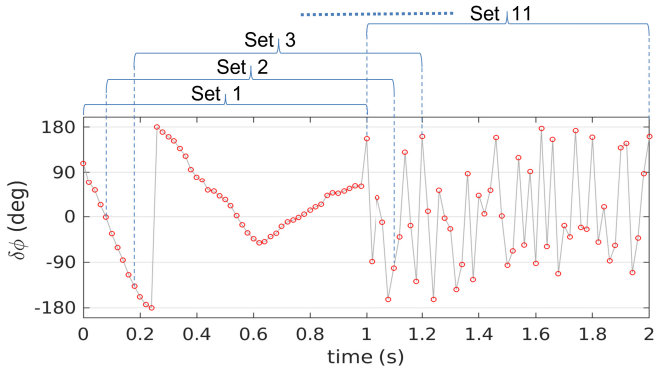


Fig. 3. 2 s of excess-phase $\delta\phi$ observations with the first 1 s being coherent followed by 1-s noncoherent data. From these 2-s data, we created 11 sets using a 1-s sliding window sliding at 0.1-s increment.

Fig. 4 shows the scatter plots of the phase rate and phase noise mean circular length $\bar{\zeta}$ versus mean circular kurtosis $\bar{K}$, as well as their $1\sigma$-standard deviation of the 11 sets of data for six added noise levels: 0°, 18°, 45°, 72°, 108°, and 162°. Without additional noise (0°), the phase-rate indicators show the largest separation in ($\bar{K}$ and $\bar{\zeta}$) for all 11 sets of data. As the noise level increases, the mean values decrease, while their standard deviations increase, and the values for the datasets also become closer to each other. At the noise level 162°, all the sets are noncoherent. The mean circular lengths for the phase rate $\delta\dot{\phi}$ and phase noise $\epsilon_{\delta\phi}$ fall in the ranges (0.1, 0.35) and (0.3, 0.6), respectively. Based on examinations of the CubeSat data, a reasonable range of noise is between 45° and 72°. Fig. 4 shows that the $\epsilon_{\delta\phi}$ indicator is more sensitive to the coherency content of the signal and is, therefore, selected as the coherency indicator in this study.

### D. Coherency Classification Based on Phase Noise Circular Statistics

Based on the discussions above, we focus on using phase noise circular statistics as a coherency indicator to classify the three regimes of coherency over a 1-s segment of Spire CubeSat observations: coherent, semicoherent, and noncoherent. A coherent segment allows precise range estimation of the reflected signal. A noncoherent segment is dominated by noise. When a segment is semicoherent, it contains a mixture of coherent and noncoherent observations. It can be viewed as "noisy" coherent measurements with a higher probability of carrier phase cycle slips [50]. The question is: what are the boundary values of the circular statistics that define these three regimes?

To obtain the boundary values, we compute the phase-noise statistics over nonoverlapping 1-s segment data listed in Table I. Fig. 5 shows scatter plots of $\zeta$ and $K$ for reflections

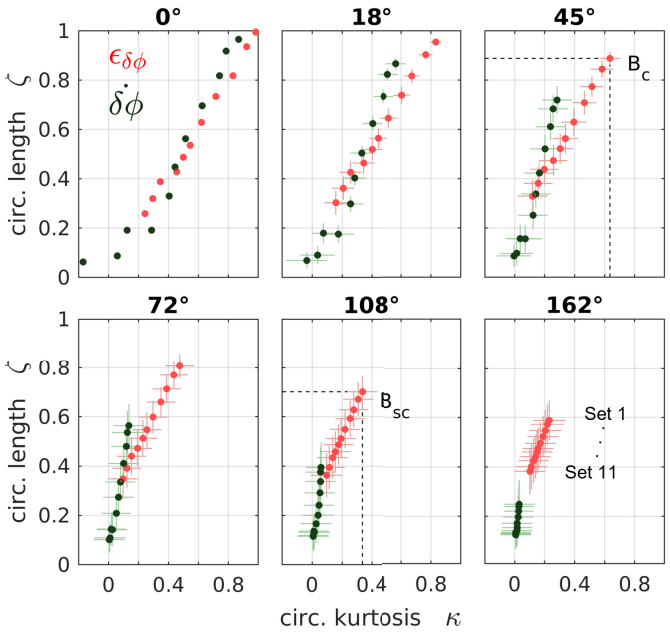


Fig. 4. Evolution of the circular statistics parameters for $\epsilon_{\delta\phi}$ (red) and $\dot{\delta\phi}$ (green) with the 11 sets of data segments shown in Fig. 3 as a function of added excess-phase noise. On each plot, for both phase noise and phase rate indicators, set #1 (coherent) is on (top right), and set #11 (noncoherent) is on (bottom left). The scatter plots show $(\bar{K}, \bar{\zeta})$ and their 1-$\sigma$ error. The added Von Mises noise level for each plot is labeled. The points $B_c$ and $B_{sc}$ are the coherent and semicoherent boundaries discussed in Section III-D.

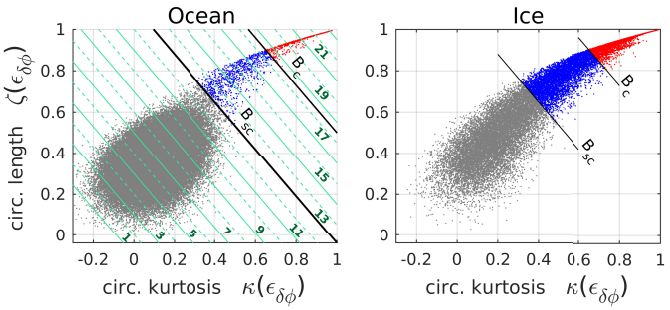


Fig. 5. Scatter plots of phase-noise $\epsilon_{\delta\phi}$ circular statistics for nonoverlapping 1-s data segments over (Left) ocean and (Right) sea ice. In the ocean scatter plot, there are 24 green lines, which delimits 23 zones; each has a corresponding set of $P_1(z)$ and $P_3(z)$ values. The line marked $B_{sc}$ defines the lower boundary of semicoherent reflection, and the line marked $B_c$ defines the boundary between coherent and semicoherent zones. The same boundaries are marked in the sea-ice scatter plot to separate the coherent, semicoherent, and noncoherent regimes.

over the ocean and sea ice. The parallel lines in Fig. 5 divide the data points into "zones." A higher zone value corresponds to higher $\zeta$ and $K$ values that are characteristic of more coherent reflections.

To obtain a more quantitative indication of the coherency level, we define $P_1(z)$ and $P_3(z)$ as the probability of having at least one- and three-cycle slips, respectively, within a zone $z$. For the 23 zones shown in Fig. 5 (left), we estimated the number of cycle slips in each 1-s segment and computed $P_1(z)$ and $P_3(z)$ values. A cycle slip is declared if the unwrapped phase change exceeds 0.7 cycles within ten phase samples. The results are plotted in Fig. 6. Based on the plot, we heuristically

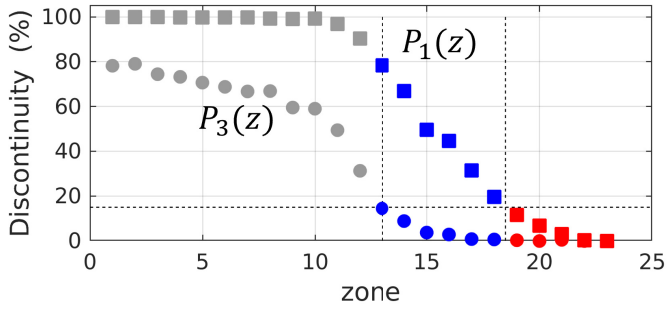


Fig. 6. Probability of a discontinuity within a second of excess-phase observations (segment) with characteristics ($K$ and $\zeta$) that belong within a zone. There are 23 zones delimited by the green lines in Fig. 5(a). The squares (circles) are the probability that there is at least 1 (respectively, 3) discontinuity in one segment of $\delta\phi$. The 15% dotted line level is the threshold chosen to delimit the noncoherent (gray), semicoherent (blue), and coherent (red) regions.

set the boundary $B_{sc}$ at Zone 13 and $B_c$ near Zone 19. Data points above $B_c$ are considered coherent, and data points above $B_{sc}$ but below $B_c$ are considered semicoherent. The $B_c$ boundary represents the data segment that has $P_1(z) = 15\%$, while $B_{sc}$ boundary corresponds to $P_1(z) = 80\%$ and $P_3(z) = 15\%$. Based on the boundaries defined by $B_c$ and $B_{sc}$, the percentage of cycle slips contained by 1-s coherent segment is 15%, by semicoherent reflection is between 15% and 80%, and by noncoherent reflections is more than 80%. These boundary values are used to classify the data points in Fig. 5: into coherent, semicoherent, and noncoherent for the ocean and sea ice.

The boundary values set above also have correspondences with the noise levels, as shown in Fig. 4. For example, $B_c$ maps to $\zeta = 0.9$ and $K = 0.63$ in Fig. 4, which corresponds to the coherent data segment 1 in Fig. 3 with a 45° added Von Mises noise. $B_{sc}$ maps to $\zeta = 0.72$ and $K = 0.35$ in Fig. 4, which corresponds to the coherent data segment 1 in Fig. 3 after adding 108° Von Mises noise.

We further plotted the PDFs of $\zeta$ and $K$ for the data collected over the ocean and sea ice on a log scale in Fig. 7. Over the ocean, the dominant noncoherent distribution ends around ($K = 0.4$; $\zeta = 0.6$), while over sea ice the coherent part starts around ($K = 0.7$; $\zeta = 0.8$). Furthermore, the extracted distributions of the coherent and semicoherent intervals appear to follow bell-curve features that again enhance the validity of this classification. Note that the bell curves are slightly better defined in the circular-length domain.

The boundary values are also consistent with the altimetry retrieving results. Data segments that fall within the coherent regime defined by the boundary value $B_c$ resulted in consistent high precision altimetry results. Data segments from the semi-coherent reflections zones contain weak coherent components that can be easily perturbed by the diffusive scattered signals. For semicoherent reflections, the phase estimations contain range information but have a low level of cycle slip corruption, which can be filtered for precise altimetry applications [50].

Table III summarizes the boundary conditions for the two coherency indicators. In addition, the coherency test requires a Spire L2 reflection signal SNR > 15 v/v. This value is

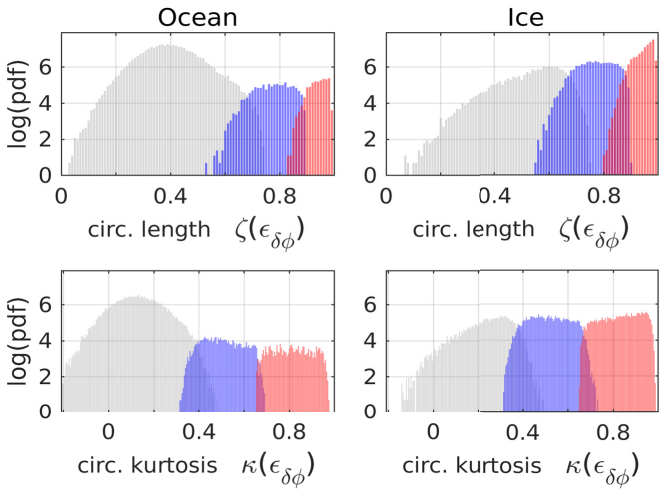


Fig. 7. PDF of (Top) $\epsilon_{\delta\phi}$ circular length and (Bottom) kurtosis for reflections over (Left) ocean and (Right) sea ice. The data are divided according to noncoherent (gray), semicoherent (blue), and coherent (red) detection results.

TABLE III
CIRCULAR STATISTICS COHERENCY BOUNDARY VALUES

| Indicator | $\epsilon_{\delta\phi}$ | $\delta\dot{\phi}$ |
|---|---|---|
| Coherent lower boundary | $\zeta = -1.15(K-0.75)+0.8$ | $\zeta = -0.5(K-0.4)+0.8$ |
| Semicoherent lower boundary | $\zeta = -1.15(K-0.6)+0.43$ | $\zeta = -0.5(K-0.24)+0.4$ |

chosen as the mean + one-standard deviation of the noncoherent ocean SNR (zones 1–11). Over sea ice, the value is in the same range. Our analysis indicates that the L2 SNR criteria and the phase noise statistics test yield consistent classification 92% of the time. Close to the boundary zones, there is not always a one-to-one correspondence for levels of coherency between the phase noise and phase rate indicators. However, the total number of coherencies (including both semicoherent and coherent) is similar. For instance, 4% of the semicoherent data classified by $\epsilon_{\delta\phi}$ is treated as noncoherent using $\delta\dot{\phi}$ statistics and vice versa. The discrepancy typically happens at the end of a coherent section. Whether to discard these data as noncoherent will depend on the results of altimetry profile validation studies (see Section V). The results provided in Section IV are based on the $\epsilon_{\delta\phi}$ indicator.

## IV. COHERENCY DETECTION RESULTS

### A. Coherent Signal SNR, Elevation, and Duration

We applied the boundaries defined above to classify data collected by Spire CubeSats. The coherent and semicoherent reflection signal SNRs, the incident signal elevation at the SP, and the coherency duration that is computed by aggregating consecutive 1-s segments are analyzed for the ocean and sea-ice surface reflections, respectively. Table IV summarizes the detection results based on the phase-noise coherency indicator. A total of 2066 and 476 reflection events were analyzed over the ocean and sea ice, respectively. Among them, 126 and 215 have coherent and semicoherent segments over the ocean, respectively, while 294 and 346 contain coherent and semicoherent segments over sea ice, respectively. It is clear that a larger percentage of the coherent events occurs over sea ice than over the ocean.

*1) Coherency Occurrence Rate:* There are a total of 540 985- and 50 631-s data for oceans and sea ice, respectively. For ocean reflections, 0.4% are coherent, and 0.6% are semicoherent. This is in contrast over sea ice where 23.5% are coherent and 20.8% are semicoherent. The total length of coherent reflections is more than 10% higher than that of the semicoherent reflections over sea ice compared to being 33% lower over the ocean.

*2) Coherency Dependence on SNR:* Fig. 8 shows the global maps of the SP tracks of detected coherent and semicoherent reflections. The left map is color-coded according to the type of surface (ocean and sea ice) and coherency level (coherent and semicoherent) determined by the phase noise circular statistics. The right map is color-coded according to the reflected signal SNR at the L2 band. Comparison between the two maps indicates that, in general, the higher L2 SNR values obtained in the Spire data correspond to more coherent reflections. However, there are deviations from this relationship as shown by the green tracks in the map on the right, which are associated with reflections that are noncoherent according to the circular statistics but whose SNR values are greater than 18 v/v.

To obtain a more quantitative relationship between coherency levels and the reflection signal SNR, Fig. 9 plots the number of 1-s coherent and semicoherent segments (left) and their accumulated occurrence rate (right) for the ocean and sea ice as a function of reflected L2 signal SNR. For both ocean and sea ice, the coherency rate increases with the SNR. Based on the occurrence plot, 80% of the reflection is coherent or semicoherent for SNR $>$ 35 v/v over sea ice. Over the ocean, to have 80% coherent or semicoherent reflections, the SNR must be over 45 v/v. For SNR at 25 v/v, about 20% and 50% of the reflections are coherent or semicoherent over the ocean and sea ice, respectively. To use a detection theme based on the SNR threshold, such as SNR $>$ 40 v/v, would miss valuable information captured at lower SNR levels and sometimes misinterpret high SNR segments with coherency, especially below 60 v/v.

*3) Coherency Dependence on Elevation Angle:* The coherency dependence on elevation has been analyzed in [29]. The conclusion still holds true here even though the coherency indicator is different. For both surface types, the probability of coherency decreases with increasing incident signal elevation angle. This is expected because the relative surface roughness decreases with elevation. In addition, at grazing angles, the RHCP component of the reflected signal is expected to be increasingly dominant with decreasing elevation over both surface types. Consequently, the reflection signal power for the RHCP antenna on Spire CubeSats is higher at a lower elevation, which may enable better detection of coherent signals at lower elevation [33].

TABLE IV
SUMMARY OF COHERENT MEASUREMENTS BASED ON GPS L2 PHASE-NOISE CIRCULAR STATISTICS

| Surface type | # of events | # of events with coherent and semicoherent reflections | | # of seconds collected | % coherent and semicoherent reflections | |
|---|---|---|---|---|---|---|
| | | Coherent | Semicoherent | | Coherent | Semicoherent |
| Ocean | 2066 | 126 | 215 | 540,985 | 0.4% | 0.6% |
| Sea ice | 476 | 295 | 346 | 50,631 | 23.5% | 20.8% |

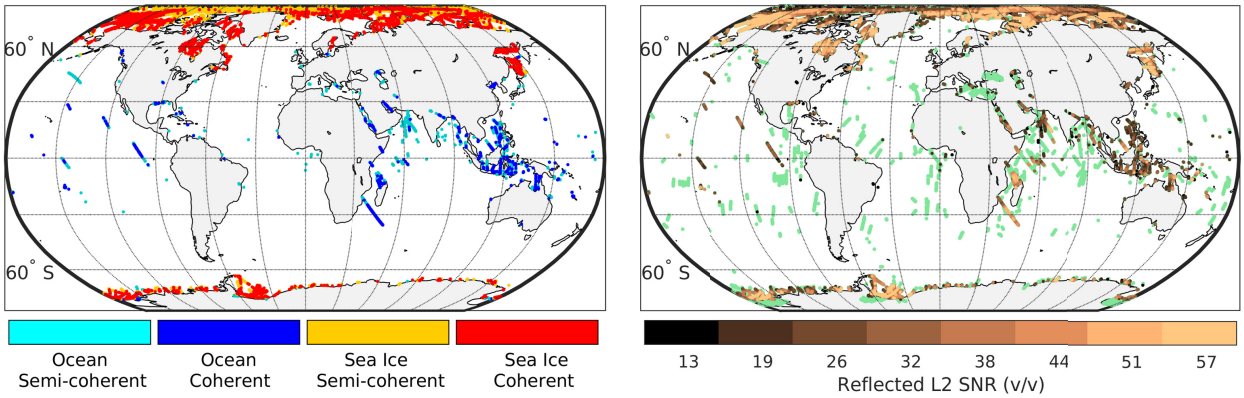


Fig. 8. (Left) Tracks of the 1-s coherent reflection SP tracks color-coded according to the reflection surface type (ocean and sea ice) and coherency type (coherent and semicoherent). (Right) L2 SNR. The green tracks are not coherent based on the phase noise circular statistics indicator but have SNR > 18 v/v.

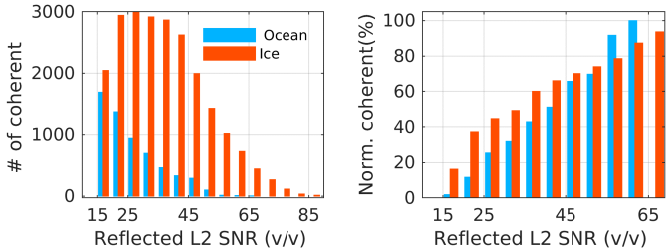


Fig. 9. Reflection signal coherency dependence on received mean L2 signal SNR for ocean (blue) and sea ice (orange). (Left) Number of coherent reflection (including semicoherent) seconds. (Right) Occurrence rate of coherent reflections normalized by the total number of coherent and noncoherent observations within each SNR bin.

*4) Coherency Duration:* The duration of coherency, as computed by aggregating consecutive 1-s coherent segments, is longer over sea ice. On sea ice, 25% coherent or semicoherent observations are over 1 min compared to 2% over the ocean, where most durations are less than 10 s.

The coherency duration is also dependent on the sea state and incident signal elevation. Fig. 10 is a scatter plot of SWH versus coherency duration, and the data points are color-coded according to the incident signal elevation. The figure shows that, while there is a widespread SWH for the short coherent duration, a longer duration is associated with relatively low SWH. Coherent reflections at higher elevations predominantly occur when the SWH is low and their duration is relatively short.

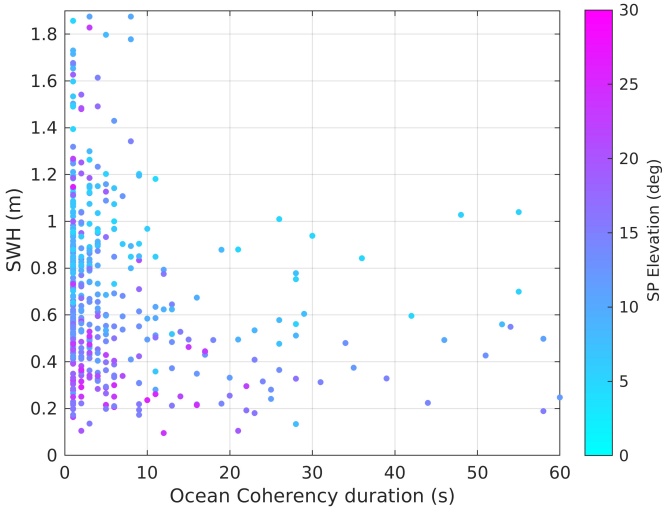


Fig. 10. Scatter plot of SWH versus coherency duration and the data points are color-coded according to the incident signal elevation.

## *B. Coherency Spatial Distribution and Dependence on Wind Speed and SWH*

Fig. 8 clearly shows that, other than a few exceptions off the northwest coast of the USA and one to the east of South Africa, most coherent and semicoherent reflections occur near coastal areas. Previous studies have shown that coherent scattering is more prevalent in areas, such as the Seas of Indonesia, where the wind speed is in general low [9], [51]. Our analysis confirms the previous findings. The areas encompassing the Pacific Ocean and East Indonesian Seas are characterized by relatively high coherency occurrence. This is correlated with the relatively low wind speed in these areas. Fig. 11(a) plots the SP tracks of the coherent and semicoherent reflections in the area. The area defined by the red rectangle is the Indonesian Archipelago within which the coherency rate is even higher. Fig. 11(b) shows the probability of low wind speed in the same region. The two maps show that the coherent tracks occur more frequently in regions of a high probability

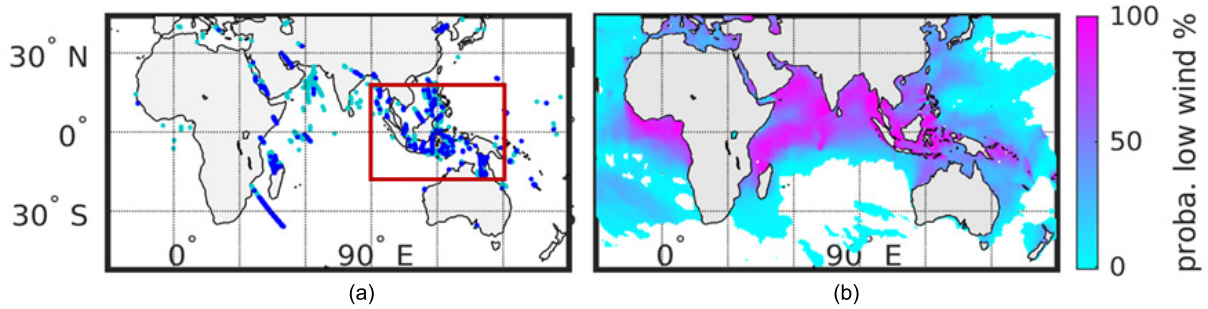


Fig. 11. (a) SP tracks of coherent (blue) and semicoherent (cyan) reflections in low latitude ocean areas with an outlined area over the Indian Ocean and Indonesian Seas. The red inset defines the Indonesian Archipelago region. (b) Probability of low wind (<7 m/s) occurrence over the days when the three-month Spire Global data were collected.

TABLE V
RATE OF COHERENT AND SEMICOHERENT REFLECTIONS DEPENDENCE ON WIND SPEED WITHIN 200 KM FROM COASTLINES

| Wind Speed Limit (m/s) | None | <6 | <7 | <8 |
|---|---|---|---|---|
| Worldwide | 5.5% | 15% | 13% | 10% |
| Pacific and East Indonesia Seas | 9% | 18% | 15% | 13% |
| Indonesian Archipelago | 11% | 23% | 20% | 18% |

of low winds and low SWH. The thresholds used to create the map of low wind occurrence are 7-m/s wind speed and 1.5-m SWH, similar to values used in [9].

Table V lists the coherent and semicoherent reflection occurrence rate within 200 km from coastlines and under three wind speed thresholds (6, 7, and 8 m/s) worldwide, the Pacific and East Indonesia Seas area, and the Indonesian Archipelago. The local SWH threshold is 1.5 m.

Note that low wind speeds are not a sufficient condition for coherency. For instance, the presence of ocean swells or oil slicks modifies the surface roughness regardless of the local instantaneous wind speed, and the local SWH depends on the history of the winds over the previous hours.

To perform a more quantitative analysis of the coherency dependence on wind speed, we identified collocated ASCAT wind speed measurements with the detected coherent reflection from the Spire data. The ASCAT data cover 1800-km-wide swaths and are sampled every 25 km along its track. We define collocated ASCAT measurements as data gathered within 2 h and 20-km radius of Spire ocean data. We sampled the Spire data over 5-s intervals, which translates into an along-track sampling ~25 km. The coherency level of these intervals is set to the maximum coherency level among 5 s of data. This led to 18 500 collocated 5-s intervals. Fig. 12 (top) shows the signal SNR versus wind speed derived from collocated ASCAT data for incident signal elevations in 5° bins. The plots illustrate that, for a given satellite elevation bin, the SNR decreases for increasing wind speed until the SNR reaches the cutoff level of ~15 v/v, below which the signal is too weak to contain any information. As the satellite elevation bin increases from the [5°–10°] bin to the [25°–30°] bin, the peak SNR values within the bins decrease from ~50 to 20 v/v, while the wind speed corresponding to the cutoff SNR value also decreases.

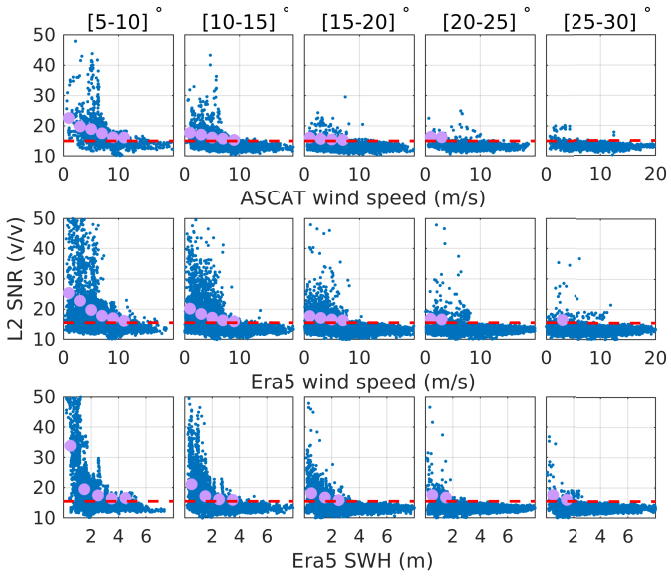


Fig. 12. Scatter plots of L2 SNR versus (Top) ASCAT wind speed, (Middle) ERA5 wind speed, and (Bottom) ERA5 SWH binned according to satellite elevation at the SP. The ASCAT wind speeds are colocated with the Spire SP within 40 km and 2 h of each other. The red dotted lines are the 15-v/v SNR level. The lavender circles are the median SNR for data points with SNR >15 v/v within a 2-m/s bin for wind speed and 1-m bin for SWH.

Because only a limited set of coherent Spire reflections has collocated ASCAT wind speed data, we obtained European Centre for Medium-Range Weather Forecasts (ECMWF) ERA5 hourly reanalysis data of wind speeds on 0.25° × 0.25° grids and SWH on 0.5° × 0.5° grids [52], [53]. We limit the wind speed data to be within the latitudes range of [−60° 40°], which contains 74 000 5-s data segments. The relationship between the Spire SNR binned by elevation and ERA5 wind speeds behaves similar to the ASCAT wind speeds, as shown in Fig. 12 (middle). We also have the L2 SNR versus SWH for the same satellite elevation angle bins, as shown in Fig. 12 (bottom). Here, the SNR decreases with increasing SWH until it reaches the background level of ~15 v/v. As the satellite elevation bin increases from [5°–10°] to [25°–30°], the peak SNR values decrease from over 50 to 35 v/v, while the SWH corresponds to the cutoff SNR decreases from ~4 to ~1.5 m. Those levels are somewhat high, most likely due to increased uncertainty in the SWH values provided by ERA5. Increasing

the background SNR level from 15 to 18 v/v would decrease the SWH cutoff from 0.5 to 2 m.

If we assume that ocean data with SNR >15 v/v correspond to reflections over low wind/wave type surfaces, then only 10% of the data under low wind/wave conditions are coherent according to Fig. 12. They occur mainly close to shore with a one-sigma distance from the coast being less than 100 km. This result over the global ocean is much less than the 33% mentioned in [9], which is based on the CYGNSS carrier-phase observations in a restricted region around Central America with signals at low grazing angles and data collected under low wind/wave conditions. Note that we heuristically selected 15 v/v as the background wind threshold value based on the lowest SNR from the ocean coherent class and the ASCAT wind speed trend. The ERA5 data seem to indicate that a higher background wind threshold level of 18 v/v is more reasonable. With these higher threshold values, the global statistic reaches 30% of the data over low wind/wave conditions are coherent.

### C. Coherency Dependence on Incident Signal Elevation

The upper two figures in Fig. 13 show that most of the wind speed for coherent reflections is below 7 m/s with a few values up to 8.5 m/s regardless of incident signal elevation at the SP, while the upper SWH levels decrease with elevation from about 2 to 0.5 m. The strongest SNRs occur at low grazing angles and low wind speeds, which is consistent with the theory. In particular, the ocean reflection below Brewster's angle of ∼7° is dominantly RHCP, which increases the SNR because the Spire antennas have an RHCP configuration. The bottom two figures in Fig. 13 emphasize that the coherency levels are not always related to the SNR levels, and regardless of elevation, higher coherency levels are observed mainly in the lower SWH boundaries. We get the same pattern using ASCAT-Spire collocated coherent events though the number of collocations is low (150 versus 1000 for ERA5).

We also looked at the coherency dependence on the ERA5 sea wave periods. The trend for the wind-wave period and swell-wave period versus elevation over the coherent ocean resembles the ones for wind-speed and SWH, respectively. Over coherent seconds, the wind-wave periods <4 s have no dependence on elevation, whereas the swell-wave periods have a dependence on elevation, with larger periods up to 10 s found at lower elevations and restricted to 4 s at 25° (not shown).

### D. Sea-Ice Spatial Patterns and Coherency Dependence on Ice Age

Table IV shows that 44.3% of the reflections over sea ice are coherent or semicoherent. To better visualize the coherency spatial patterns, the SP track over the Arctic is shown in two one-month periods in Fig. 14. The first period is from January 8 to February 10 collected by Spire SVN 090 and 086 [see Fig. 14(a)]. The second is from March 15 to April 11 with data from Spire SVN 086 [see Fig. 14(b)]. Coherent (red), semicoherent (black), and noncoherent tracks (blue) are shown in the plots. The first period shows more coherent tracks than the second period. During both periods, the central

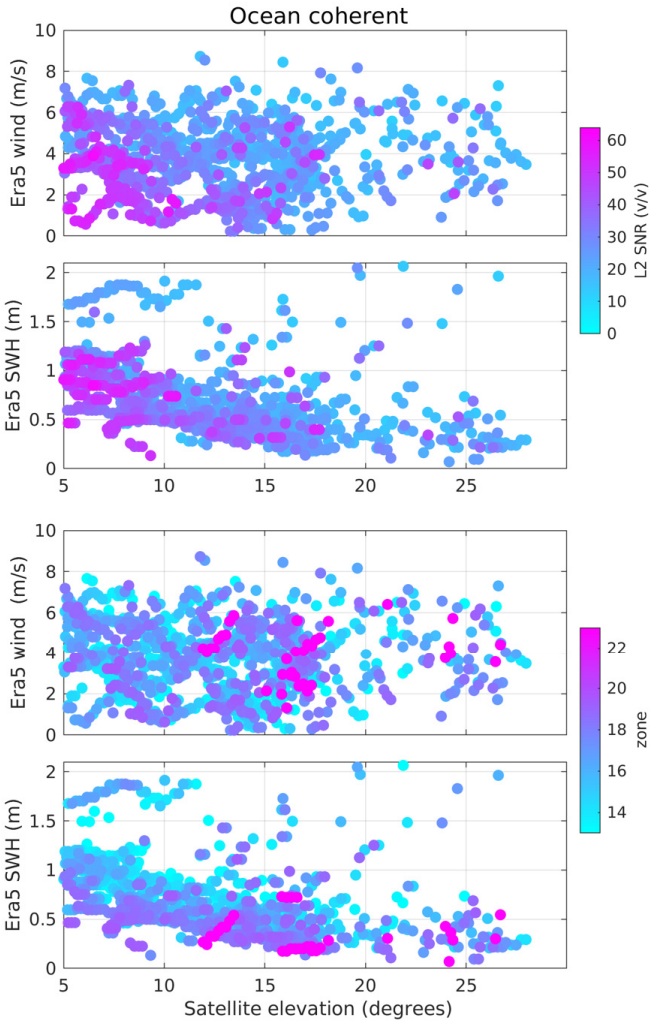


Fig. 13. (Top Two Figures) Scatter plot of (Top) ERA5 wind speed and (Bottom) SWH versus elevation at the SP for coherent and semicoherent segments of data. The plots are color-coded with mean L2 SNR values. (Bottom Two Figures) Same as above, but the plots are color-coded according to the "zones" shown in Fig. 5. The coherency level starts at zone 13 (semicoherent lower limit) and goes up to 23 (upper coherent limit).

TABLE VI
ARCTIC (LATITUDE > 70 °N) COHERENCY CLASSIFICATION ACCORDING TO ICE AGE

| Coherency type | Ice age <=1 year | Ice age >1 year |
|---|---|---|
| Coherent | 35% | 7% |
| Semicoherent | 25% | 22% |
| Noncoherent | 25% | 71% |

section around the North Pole is less coherent. This less coherent central area corresponds to the location of the MY sea ice, obtained from NSIDC [54] [see Fig. 14(c)]. As the sea-ice ages, the coherency level of the reflections decreases. Fig. 14(d) plots the percentage of coherent and semicoherent reflections based on the three types of coherency tracks, as shown in Fig. 14(a).

We further quantify the coherent and semicoherent events classification according to sea-ice age. Table VI lists the results

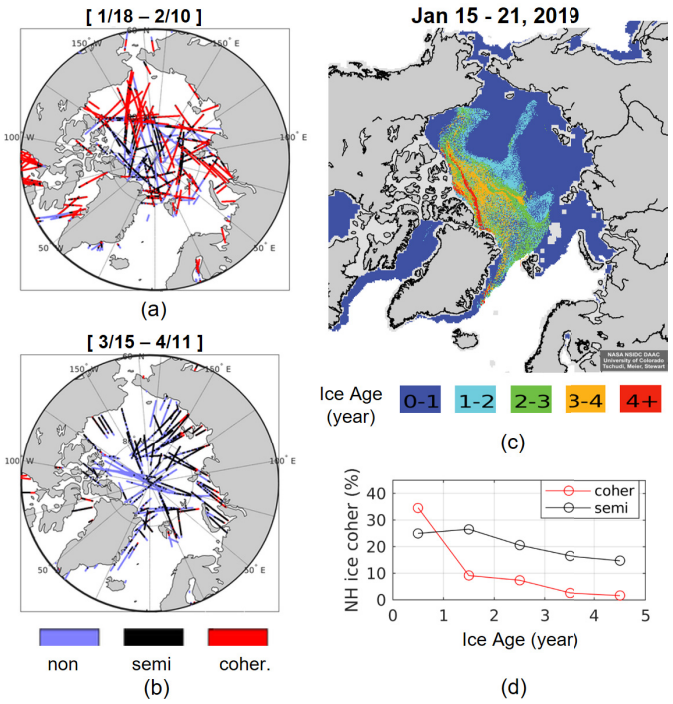


Fig. 14. SP tracks over the Arctic sea ice for (a) 1/8 to 2/10, 2019, and (b) 3/5 to 4/11, 2019, color-coded by coherency levels (noncoherent, lavender; semicoherent, black; and coherent, red). (c) Arctic sea-ice age from NSIDC [54] during the third week of January. (d) Percentage of sea-ice coherency as a function of ice age over the Arctic based on the tracks shown in (a) and (b).

for reflections occurred above 70 °N latitude. The ice age is obtained from the NSIDC map. For reflections over FY ice surface, 35% are coherent, 25% are semicoherent, and 25% are noncoherent. For MY ice, only 7% of reflections are coherent, 22% are semicoherent, and an overwhelming 71% are noncoherent. This trend is also evident in Fig. 14(b) where the coherent data are almost nonexistent when the FY ice became older and thicker than in the first period. This is consistent with the results provided in [55] that shows how sea-ice roughness extracted from reflected GPS signals increases as the ice age increases from new to MY ice. MY ice has low salinity content, and its surface is weathered by the melting ponds. The smooth high-salinity content of new-ice roughens as it drifts and is being pushed by winds and currents, collides, and piles up. The sea-ice dominant LHCP reflectivity at moderate elevation angle decreases with ice age [55]. Rodriguez-Alvarez *et al.* [56] use these properties to successfully classify sea ice using the GNSS scattering information from the DDMs collected by TDS-1 over the Arctic. The Spire data indicate that the ice conditions during the initial growth season seem to be able to provide long continuous coherent tracks. More Spire data from a complete growth/melt ice season and comparisons with other sea-ice products are needed to test under which sea-ice surface conditions coherent reflections occur. These conditions may be specific to the low grazing angle setting and RHCP antennas of Spire CubeSats, which is different from the sea-ice coherent reflections collected on TDS-1 with an LHCP antenna at moderate elevation angle [25]. In particular, sea-ice reflected signals become dominantly RHCP for grazing angles less than Brewster's angle with typical values 30° and 18° for MY/FY and Young Ice, respectively, at GPS L-band frequencies [35], [36].

### *E. L1 and L2 Reflection Signal Characteristics Comparison*

We apply the same phase noise circular statistics as the coherency test to signals over the ocean and sea ice. The Spire L1 carrier phase estimations must be corrected for half-cycle jumps that arise from the 50-Hz navigation data modulation. The navigation data are removed by aligning the estimated phase with the known data bit stream retrieved from the bit grabber network (bitArc) of Constellation Observing System for Meteorology, Ionosphere, and Climate (COSMIC) [57]. Out of the initial 2500 events, navigation data bits were successfully removed from 1800 events. Note that the L1 SNR is not affected by this correction. In the following, we compare the SNR and coherency indicators generated from L1 and L2 measurements.

*1) L1 and L2 Reflection Signal SNR Comparisons:* The variations in reflected signal SNR are in part due to the roughness and the electric permittivity of the ocean surface, as well as the GPS and LEO satellite antenna gain patterns. Higher SNRs are typically associated with more coherent reflections, but deviations from this trend do occur, as discussed in Section III. The generally accepted rule of thumb is that noncoherent reflections correspond to SNR $<$ 20 v/v on L1 or SNR $<$ 15 v/v on L2. Typically, L1 SNRs are higher than that of L2. However, the Spire L1 SNR fluctuates more. Our survey of the three-month Spire data shows that, for L2 SNR values above 15 v/v, the average L1 and L2 SNRs are 31 and 25 v/v, respectively. The standard deviation for L1 SNR is 21 v/v, which is 70% of its mean value. In contrast, the L2 SNR standard deviation is 12 v/v, about 50% of its mean. Larger fluctuations in the L1 SNR imply more risks of cycle slips in the phase estimation [58].

An example of the SNR time series from a reflection event over the South China Sea is presented in Fig. 15. The event lasted 180 s, and the satellite elevation at the SP decreased from 15° to 7°. The L2 SNR starts at ∼25 v/v, reaching a first peak ∼45 v/v, before it returned to just above the baseline followed by another peak. According to the circular statistics shown in the bottom plot, the L2 reflection was semicoherent once the SNR reached 30 v/v and became coherent over the second plateau. The dip between the peaks is almost at the baseline level, but it is classified as semicoherent because it occurred at a lower elevation angle when the effective ocean roughness was reduced.

The L1 SNR fluctuation patterns follow that of the L2 SNR but at an enhanced level. Even though L1 SNRs are higher, comparison between L1 and L2 circular statistics shows that, overall, the L1 signal does not provide additional coherent information over the L2 except over a 2-s period, whereas L2 offers an extra 52 s of coherency relative to L1.

Fig. 16 further illustrates the evolution of a 14-s segment dual-band excess-phase observations reflected over sea ice. In this case, the L2 SNR is higher than that of L1, and the L2 circular statistics are also above that of L1.

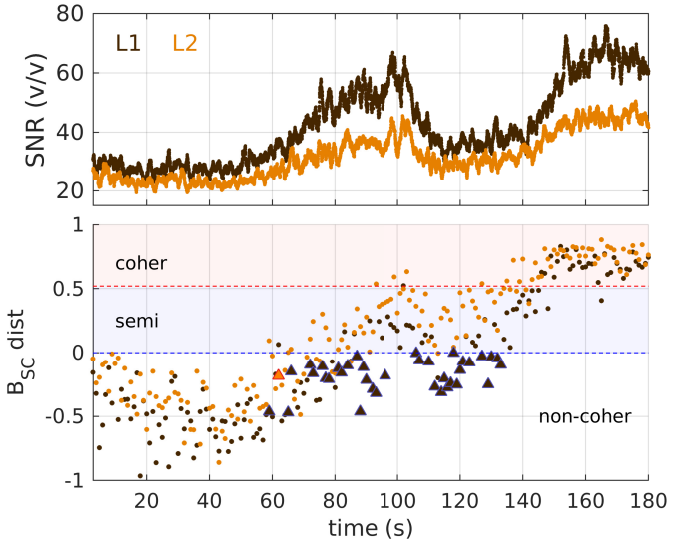


Fig. 15. Example Spire reflection event over South China Sea of GPS PRN 10 signals reflection collected by Spire SVN 084. The satellite elevation angle decreases from 15° to 7°. (Top) L1 (black) and L2 (yellow) SNR. (Bottom) $\epsilon_{\delta\phi}$ circular statistics converted to the signed distance from the semicoherent boundary level $B_{\rm sc}$. This distance is normalized so that $(K, \zeta) = (1, 1)$ for complete coherent reflection. A negative value means that the data are noncoherent. The semicoherent signal corresponds to 0∼0.5. The dots in the bottom plot represent the cases where L1 and L2 have the same coherency classification. There are clusters of dark triangles representing the cases where L1 is noncoherent, while L2 is coherent. There is only one yellow triangle, which represents when L2 is noncoherent, while L1 is coherent.

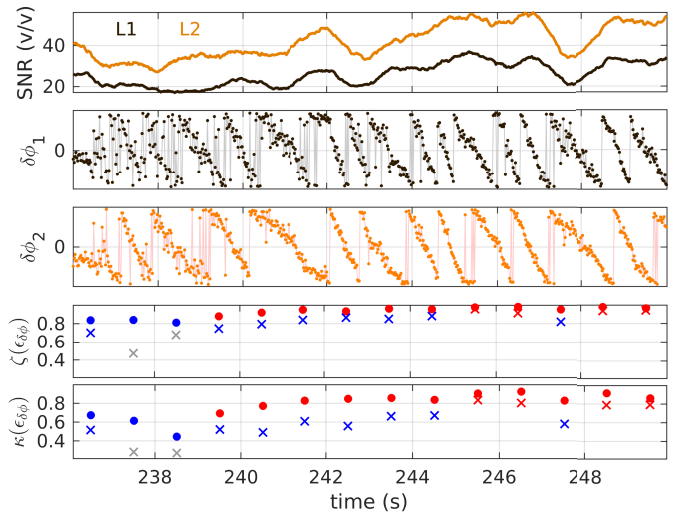


Fig. 16. Example GPS PRN 26 L1 and L2 reflection signal excess phase over sea ice obtained from Spire SVN 090 on February 4, 2019, with 0 s at 10:15:32 UTC. From top to bottom: SNR; L1 excess phase $\delta\phi_1$; L2 excess phase $\delta\phi_2$; and $\epsilon_{\delta\phi}$ circular length and kurtosis statistics over 1-s data (x for L1 and o for L2, red for coherent, blue for semicoherent, and gray for noncoherent.

*2) L1 and L2 Reflection Signal Circular Statistics Comparisons:* Fig. 17 (top) shows scatter plots of L2 versus L1 phase-noise circular kurtosis for ocean (left) and sea-ice (right) reflections. For the ocean plot, the data points can be separated into two distinct sections: a circular area of noncoherent data with low $K$ values spanning the range of $[-0.25, 0.25]$ and an asymmetric cone-shaped extension with an apex at $K = 1$.

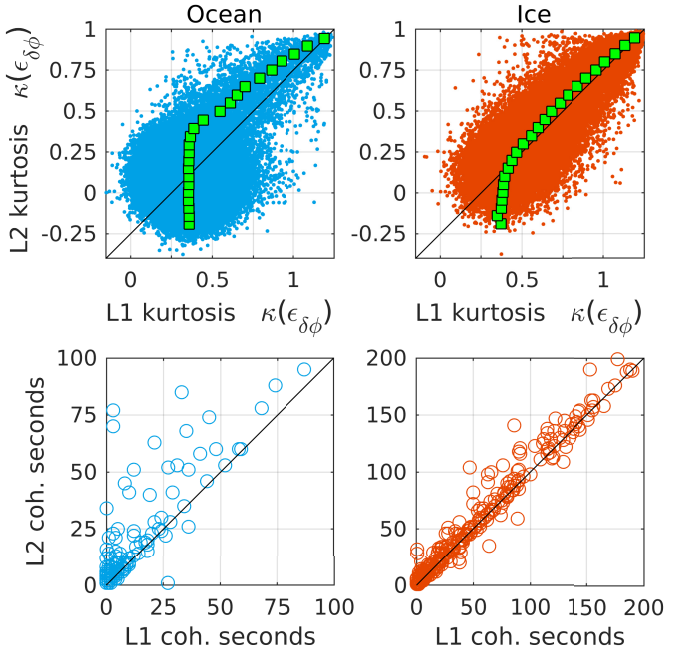


Fig. 17. (Top) Scatter plot of phase-noise $\epsilon_{\delta\phi}$ circular kurtosis $K$ for L2 versus (Left) L1 over ocean and (Right) sea ice. (Bottom) Number of L2 versus L1 coherent and semicoherent seconds in each reflection event. There are 130 (260) "coherent" events over the ocean (sea ice).

In the cone-shaped region, the L2 statistics values are higher than that of L1, as shown by the green squares that are the median of the L1 statistic computed over a data bin width of 0.05. Over sea ice, the plot is nearly symmetric around the unit line, demonstrating that L1 and L2 statistics are consistent with one another. The scatter plot of L1 and L2 phase-noise circular lengths follows the same tendency (not shown) being asymmetric in the coherent region over the ocean but almost symmetric over sea ice.

We also computed the number of seconds when L2 and L1 reflections are coherent or semicoherent for events that include at least one coherent or semicoherent second and plotted the results in Fig. 17 (bottom). Generally, L2 provides more coherent observations than L1 over the ocean. Over sea ice, L1 and L2 coherent occurrences are very close. The correlation slopes between the number of L1 and L2 coherent segments are 1.3 and 1.03 over the ocean and sea ice, respectively. Table VII summarizes the observed coherency occurrence for L1 and L2 over the ocean and sea ice and gives the coherency percentages according to whether one of the signals is coherent (L1∪L2), or both are coherent at the same time (L1∩L2). It is clear that L1 and L2 do not always show coherency at the same time. In weak coherent regions, they intermingle. However, especially over the ocean, when L1 is coherent there is a high probability that L2 will also be coherent, rather than the other way around.

## V. Coherency Classification Validation Through Altimetry Retrieval

Previous studies on the Spire data have shown that cm-level reflection surface height profiles can be obtained with better

TABLE VII
SPIRE DATA PROCESSING RESULTS CLASSIFICATION ACCORDING TO L1 AND L2 DATA

| Reflection surface type | Total # of events | # of L1 & L2 coherent and semicoherent events | Additional # of coherent and semicoherent events on L1 or L2 | | % coherent and semicoherent seconds | | | |
|---|---|---|---|---|---|---|---|---|
| | | | L1 | L2 | L1 | L2 | L1∪L2 | L1∩L2 |
| Ocean | 1495 | 130 | 5 | 15 | 0.16% | 0.95% | 1% | 0.57% |
| Sea ice | 370 | 260 | 1 | 5 | 41% | 44% | 48% | 38% |

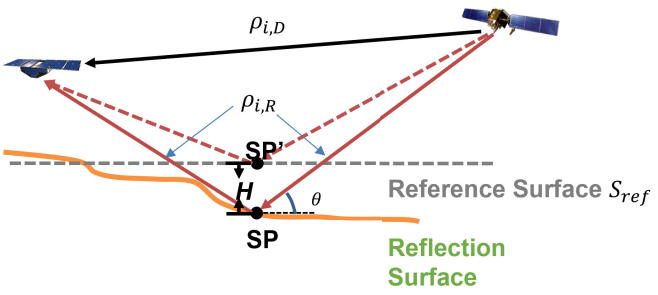


Fig. 18. Phase altimetry retrieval geometry illustration.

performance over sea ice than the ocean water [33], [58]. The goal here is to assess the soundness of the coherency level classification and evaluate the quality of the altimetry retrievals in the three coherency regimes. In this section, we first describe the process and methodology of altimetry retrieval. Retrieval results and analysis over the ocean and sea ice for coherent and semicoherent reflections are then presented.

### A. Phase Altimetry Retrieval Method

Phase altimetry retrieval is the estimation of the reflection surface height above a reference height. We achieve it by subtracting the direct signal phase measurements from the reflected signal phase measurements received on the same antenna. The procedure is similar to the ones described in [25], [33], and [58]. Fig. 18 illustrates the geometry of the retrieval. The process is summarized in the following.

*Step 1:* Obtain coherent phase estimations for direct and reflected GPS L1 and L2 signals, $\phi_L^D$ and $\phi_L^R$, by adding the unwrapped phase residuals to the accumulated input Doppler range model. Before the direct and reflected signal phase can be used for the retrieval, the L1 excess phase must be corrected from half-cycle jumps by demodulating the $I/Q$ correlation outputs with the navigation data bits. Then, the coherent quality test is performed to detect segments that contain coherent and semicoherent reflections from both reflected L1 and L2 signals.

*Step 2 (Phase Estimation Filtering):* Depending on the amount of ocean scattered signal that contaminates the coherent portion of the reflected signal, the reflected excess phase may be noisy and contain cycle slips, which creates decimeter level or larger jumps in the unwrapped phase. The Simultaneous Carrier cycle slip reduction and Noise Filtering (SCANF) algorithm described in [58] is applied to the reflection observations to mitigate cycle slips and the noise effect.

*Step 3:* Compute the bistatic path delay between the reflected and the direct signals

$$\Delta\rho_{L,\text{mea}} = \lambda_L\left(\phi_L^R - \phi_L^D\right) + \lambda_L n_L \tag{6}$$

where $\lambda_L$ is the carrier wavelength and $n_L$ is the integer carrier ambiguity term.

*Step 4:* Compute $H_L$, the surface height deviation from a reference surface $S_{\text{ref}}$

$$H_L = \frac{-\left(\Delta\rho_{L,\text{mea}} - \Delta\rho_{L,\text{mod}}\right)}{2\sin\theta} = \frac{-\Delta\rho_{L,\text{res}}}{2\sin\theta} \tag{7}$$

where $\theta$ is the GPS satellite elevation angle seen from the SP and $\Delta\rho_{L,\text{mod}}$ is the modeled bistatic path delay that includes contributions from the geometric range, troposphere delay, ionosphere advancement, and carrier integer ambiguity. Each of these terms must be corrected to retrieve $H_L$.

The geometric range is estimated based on the precise positions of the GPS satellite, the Spire CubeSat, and the predicted SP location on the reference surface $S_{\text{ref}}$. In this study, $S_{\text{ref}}$ is the combination of the DTU18 MSS [59] and ocean tide from the TPXO8 global ocean tide model [60]. The SPs are computed using the iterative approach described in [61]. The receiver position and clock bias are given in the Spire metadata from the postprocessed Spire satellite POD solution, which has cm-level precision [44]. The GPS satellite position and clock bias are derived from the IGS precise orbit data product (www.igs.org).

The tropospheric delay is estimated using the daily global grids of zenith delay and VMF3 mapping functions from the Technical University of Vienna [62]. The first-order ionospheric carrier phase advance is estimated by differentiating the L1 and L2 observations. The carrier ambiguity is removed by subtracting a bias between the measured and modeled bistatic delay residuals $\Delta\rho_{L,\text{res}}$ to minimize the RMS between $H_L$ and $S_{\text{ref}}$. Therefore, the altimetry retrieval provides a relative height profile above $S_{\text{ref}}$ along the specular track.

### B. Altimetry Retrieval Result Analysis

Datasets for each coherency regime are processed, and the retrieved relative surface height profiles are analyzed. Unlike the earlier studies [33], [58] where the reflection events last more than 1 min, the dataset used in this study consists of 30 s of observations within a specific coherency regime. The 30-s duration is a compromise that ensures a sufficient number of segments for analysis while still providing sufficient

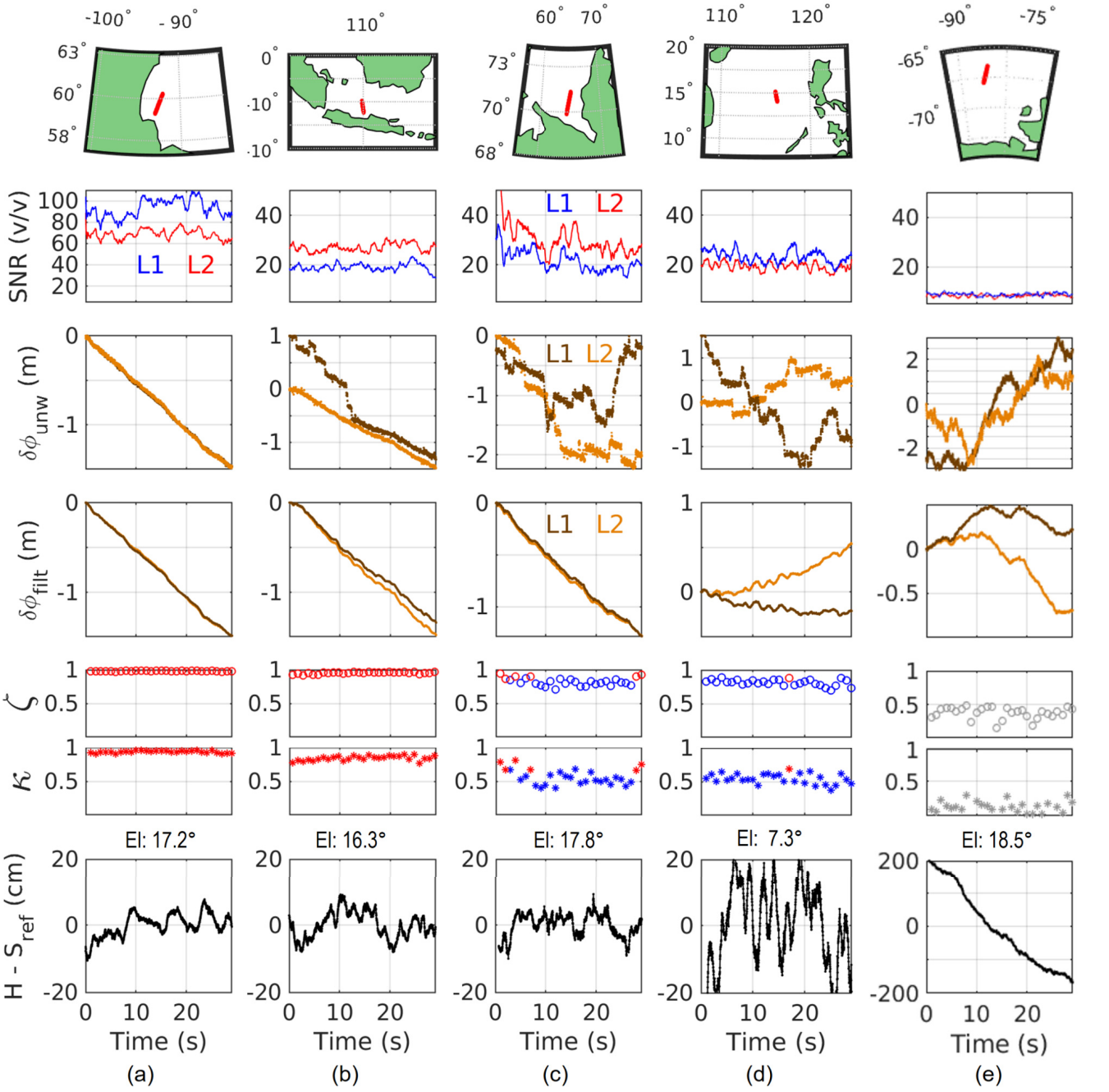


Fig. 19. Five examples of altimetry retrievals over 30-s Spire data sampled at 50 Hz shown in five columns. (a) Coherent over sea ice. (b) Coherent over the ocean. (c) Semicoherent over sea ice. (d) Semicoherent over the ocean. (e) noncoherent. The rows from (top) to (bottom) are specular track; SNR (each horizontal grid line is 20 v/v); raw unwrapped excess phase (each horizontal grid line is 50 cm); filtered excess phase; phase-noise $\epsilon_{\delta\phi}$ circular statistics (red: coherent; blue: semi; and gray: noncoherent); and altimetry height profile with mean satellite elevation angle over the specular track indicated on the plots.

observations of deviations between the retrieved surface height and the reference surface. The noncoherent regime provides a baseline when there is no information content about the reflected surface.

We found ~120 coherent and 23 semicoherent sets that have a duration lasting 30 s. The smaller number of a semicoherent segment is due to the fact that they are embedded within coherent or noncoherent segments. We randomly selected 120 sets of noncoherent segments. Fig. 19 shows example profiles for the semicoherent and coherent regimes over the ocean and sea ice, as well as one for the noncoherent regime. A summary of the key parameters and retrieval results for the five example profiles is provided in Table VIII. In the following, we examine the properties and accuracy of these example profiles.

*1) Circular Statistics:* The two coherent cases have $\epsilon_{\delta\phi}$ circular statistics parameters ($\bar{\zeta}$ and $\bar{K}$) above (0.9, 0.7), while, for the semicoherent examples, the average circular statistics

TABLE VIII
SUMMARY OF CHARACTERISTICS OF THE EXAMPLE DATASETS SHOWN IN FIG. 18

| | | (a) Coherent: sea ice | (b) Coherent: ocean | (c) Semicoherent: sea ice | (d) Semicoherent: ocean | (e) Noncoherent |
|---|---|---|---|---|---|---|
| Minimum SNR (v/v) | L1 | 90 | 18 | 20-35 | 22 | 10 |
| | L2 | 60 | 25 | 25-40 | 20 | 10 |
| GPS elevation at SP (°) | | 16.5-17.9 | 15.8-17.1 | 17.1-18.5 | 6.7 -7.8 | 17.9-19 |
| $(\bar{\zeta}, \bar{K})$ from $\epsilon_{\delta\phi}$ | | (0.95, 0.8) | (0.9, 0.7) | (0.8, 0.5) | (0.8, 0.6) | (0.4, 0.2) |
| RMS($\delta\phi_{unw} - \delta\phi_{filt}$) (cm) | L1 | 0.86 | 75 | 52 | 171 | 275 |
| | L2 | 0.93 | 1.5 | 82 | 30 | 145 |
| RMS($H - S_{ref}$)(cm) | | 3.50 | 4.25 | 4.30 | 12.30 | 116 |

are (0.8, 0.5) with minimum at (0.7, 0.4). The noncoherent case has ($\bar{\zeta}$ and $\bar{K}$) at (0.4, 0.2).

*2) Reflection Signal SNR:* Fig. 19 (row two) shows the direct and reflection signal SNR for the five example profiles. The SNR levels are above 15 v/v except for the noncoherent example where it is ∼10 v/v. For the two coherent cases, the SNRs over sea ice are above 60 v/v with L1 levels higher than L2 by 50%. For the coherent example over the ocean, the SNR levels are mostly at around 20 v/v but hit a minimum of 18 v/v toward the end of the track. The coherent ocean reflection example SNR levels are similar to that of the semicoherent example over sea ice. Also notice that the differences in L1 and L2 SNRs depend on the dataset due to a combination of factors such as the reflective surface properties, the GPS antenna transmission patterns, and the Spire CubeSat antenna gain patterns.

*3) Phase Discontinuity and Filtering:* The SNR level alone is not sufficient to distinguish the coherent regime from the semicoherent regime. In these examples, the semicoherent regime is more clearly identified by the discontinuities in the raw L1 and L2 unwrapped excess phases, as shown in the third row of Fig. 19. For the coherent cases, the L2 signal has no discontinuity, and there are only a few discontinuities for the coherent ocean case in the L1 band. For the two semicoherent cases, there are numerous discontinuities in L1 and L2. We applied the SCANF algorithm to reduce the noise and discontinuities in the unwrapped phase measurements. The results are plotted in the 4th row in Fig. 19. We use the RMS difference between the filtered $\delta\phi_{\text{filt}}$ and unfiltered $\delta\phi_{\text{unw}}$ excess phases as a measure of the improvement in phase discontinuity and noise reduction. The RMS values for the example profiles are listed in Table VIII. The improvement is clearly most prominent for semicoherent reflections although the L1 coherent ocean reflection also required extensive repair. In addition, the effect of the ionosphere can be clearly observed by the divergence in $\delta\phi_{\text{filt}}$ between L1 and L2, and can be removed using the difference of the filtered dual-frequency phase estimations.

*4) Relative Surface Height Retrieval:* The bottom row of Fig. 19 shows the relative surface height retrieval results. The coherent height profiles have an RMS difference of a few centimeters at 50-Hz sampling. The semicoherent examples over sea ice have comparable quality as the coherent ocean example, while the semicoherent ocean reflection RMS remains within 20 cm. Note that the SP elevation range is lower at ∼6° for the semicoherent ocean case compared to ∼16° in the other sets. This makes its height profile more susceptible to noise in the path delay variations from their $(\sin\theta)^{-1}$ relationship and larger troposphere errors. For the noncoherent case, the surface height profile shows no relation to $S_{\text{ref}}$, with a large linear trend difference of more than 10 cm/s and an RMS at the meter level, as expected.

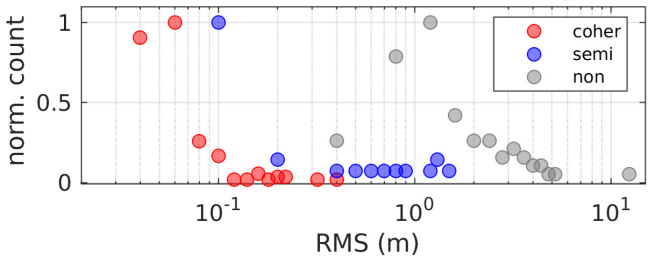


Fig. 20. Histogram of the RMS difference $(H - S_{\text{ref}})$ where $H$ is the retrieved altimetry profile over 30 s for coherent, semicoherent, and noncoherent segments.

Finally, Fig. 20 plots the histogram of the RMS height residuals for all cases and each coherency regime. It shows that the majority of the RMS are below 5 cm and above 1 m for the coherent and noncoherent regimes, respectively. The coherent and noncoherent histograms are well separated. The semicoherent regime seems to have one cluster with the decimeter level RMS values. However, depending on the amount of perturbation within the 30-s duration, the semicoherent RMS can reach the meter level. If this is the case, the semicoherent datasets can be further processed either to detect one large jump or be discarded. The median RMSs over a 30-s segment are 4.0, 8.5, and 116 cm over coherent, semicoherent, and noncoherent domains, respectively. This result indicates that the introduction of the semicoherent regime extends the condition to a broader range of measurements that can potentially yield precise altimetry height profiles. More discrimination and quality control can be achieved by studying the RMS between the raw and filtered excess phases.

## VI. CONCLUSION AND DISCUSSION

### A. Conclusion

This article presents an assessment of the coherency of grazing angle reflected GPS signals received by Spire Global

CubeSats. The phase coherency is determined using circular length and kurtosis of the excess-phase noise over 1-s segments of data. Boundary values of these two circular statistics indicators are defined to classify the reflection signal as coherent, semicoherent, and noncoherent based on the occurrence rate of carrier phase cycle slips and validated using altimetry retrieval results. A noncoherent 1-s segment has 80% and 15% or more probability of having one- and three-cycle slip occurrences, respectively, in the 1-s segment of data, while a coherent segment has less than 15% probability of having a one-cycle slip and no probability of having three-cycle slips. A semicoherent segment has statistics in between these two boundaries. Detecting the semicoherent segments is especially important over the ocean because of the relatively low percentage of data in the coherent regime. Analysis of three-month Spire CubeSat data indicates that, by combining the semicoherent and coherent reflections, 1% and 44.3% of GPS L2 reflections contain sufficient coherent energy over the ocean and sea ice for altimetry retrieval, respectively. These numbers drastically increase if we focus on ocean reflections near coastlines and the sea-ice reflections over fresh ice surfaces. For example, the worldwide combined coherent and semicoherent reflection rate is 5.5% within 200 km from coastlines. Under low wind conditions with wind speed less than 6 m/s and SWH less than 1.5 m, this number increases to 15%. In certain areas where the ocean is known to be calm, such as the Indonesia Archipelago, the combined coherent and semicoherent reflection rate can reach 23%. Our analysis also found that, while there is a strong relationship between coherency and signal SNR levels, a high SNR is not a sufficient condition for coherency. There are more coherency occurrences as the SP elevation decreases. The qualities of the L1 and L2 coherent reflected GPS signals over sea ice are similar, in contrast to noisier L1 reflected signals over the ocean. In general, the SNR levels over sea ice are stronger and the coherency duration length is longer compared to over the ocean surface. The coherency spatial patterns over sea ice also have a strong dependence on an ice age, with the fraction of coherent reflections being higher over younger, newer ice. Based on the Spire data analysis, the coherent and semicoherent reflection rate is 70% over the first year, fresh sea ice in the Arctic region. As the ice ages, this rate goes down to 32%.

Finally, this study shows that, by using postprocessing filtering methods, such as SCANF, the semicoherent reflection signals can be used to retrieve surface height with nearly the same precision as that of coherent reflection. This is especially true when the semicoherent segments are embedded within coherent ones. The inclusion of the semicoherent segments will increase the along-track length of the retrieved altimetry profile without the need to change the hardware/software onboard the LEO satellites.

### B. Discussion

The coherency analysis presented in this article is limited to the hardware and processing software quality of the Spire Global CubeSats. Better antenna gain, improved hardware calibration, and more accurate reference generation will improve reflection signal coherency rate over the ocean and sea ice. With the increasing quantities of observations, the Spire Cryosphere research group already classified sea ice over the Arctic during Spring 2020, exploiting the signature of ice age on the reflected signal using the circular length phase-rate parameter [31]. This new data collection with better temporal and spatial coverage offers the opportunity for cross-validation and precision ocean/sea-ice altimetry validation with other platforms, such as IceSat2 and Sentinel 3.

## ACKNOWLEDGMENT

The Spire data used in this study are part of the NASA Commercial Data Acquisition Program. The authors would like to thank Drs. Dallas Masters and Vu Nguyen from Spire Global for their technical support.

## REFERENCES

[1] S. Abdalla *et al.*, "Altimetry for the future: Building on 25 years of progress," *Adv. Space Res.*, vol. 68, pp. 319–363, Mar. 2021.
[2] E. D. Zaron and C. B. Rocha, "Internal gravity waves and meso/submesoscale currents in the ocean: Anticipating high-resolution observations from the SWOT swath altimeter mission," *Bull. Amer. Meteorol. Soc.*, vol. 99, no. 9, pp. ES155–ES157, Sep. 2018.
[3] R. Morrow *et al.*, "Global observations of fine-scale ocean surface topography with the surface water and ocean topography (SWOT) mission," *Frontiers Mar. Sci.*, vol. 6, p. 232, May 2019.
[4] M. Martín-Neira, "A passive reflectometry and interferometry system (PARIS): Application to ocean altimetry," *ESA J.*, vol. 17, no. 4, pp. 331–355, 1993.
[5] F. Huang *et al.*, "Sequential processing of GNSS-R delay-Doppler maps to estimate the ocean surface wind field," *IEEE Trans. Geosci. Remote Sens.*, vol. 57, no. 12, pp. 10202–10217, Dec. 2019.
[6] R. Shah, J. L. Garrison, A. Egido, and G. Ruffini, "Bistatic radar measurements of significant wave height using signals of opportunity in L-, S-, and Ku-bands," *IEEE Trans. Geosci. Remote Sens.*, vol. 54, no. 2, pp. 826–841, Feb. 2015.
[7] J. L. Garrison, S. J. Katzberg, and M. I. Hill, "Effect of sea roughness on bistatically scattered range coded signals from the global positioning system," *Geophys. Res. Lett.*, vol. 25, no. 13, pp. 2257–2260, Jul. 1998.
[8] J. Mashburn, P. Axelrad, S. T. Lowe, and K. M. Larson, "Global ocean altimetry with GNSS reflections from TechDemoSat-1," *IEEE Trans. Geosci. Remote Sens.*, vol. 56, no. 7, pp. 4088–4097, Jul. 2018.
[9] E. Cardellach *et al.*, "First precise spaceborne sea surface altimetry with GNSS reflected signals," *IEEE J. Sel. Topics Appl. Earth Observ. Remote Sens.*, vol. 13, pp. 102–112, 2019.
[10] Y. Wang and Y. J. Morton, "Coherent GNSS reflection signal processing for high-precision and high-resolution spaceborne applications," *IEEE Trans. Geosci. Remote Sens.*, vol. 59, no. 1, pp. 831–842, Jan. 2020.
[11] M. P. Clarizia, C. Ruf, P. Cipollini, and C. Zuffada, "First spaceborne observation of sea surface height using GPS-reflectometry," *Geophys. Res. Lett.*, vol. 43, no. 2, pp. 767–774, 2016.
[12] W. Li, E. Cardellach, F. Fabra, S. Ribo, and A. Rius, "Assessment of spaceborne GNSS-R ocean altimetry performance using CYGNSS mission raw data," *IEEE Trans. Geosci. Remote Sens.*, vol. 58, no. 1, pp. 238–250, Jan. 2020.
[13] M. Hoseini, M. Asgarimehr, V. Zavorotny, H. Nahavandchi, C. Ruf, and J. Wickert, "First evidence of mesoscale ocean eddies signature in GNSS reflectometry measurements," *Remote Sens.*, vol. 12, no. 3, p. 542, Feb. 2020.
[14] E. Cardellach, C. O. Ao, M. de la Torre Juárez, and G. A. Hajj, "Carrier phase delay altimetry with GPS-reflection/occultation interferometry from low Earth orbiters," *Geophys. Res. Lett.*, vol. 31, no. 10, May 2004.
[15] J. S. Löfgren, R. Haas, H.-G. Scherneck, and M. S. Bos, "Three months of local sea level derived from reflected GNSS signals," *Radio Sci.*, vol. 46, no. 6, pp. 1–12, Dec. 2011.
[16] A. M. Semmling *et al.*, "Detection of Arctic ocean tides using interferometric GNSS-R signals," *Geophys. Res. Lett.*, vol. 38, no. 4, pp. 1–17, Feb. 2011.

[17] J. S. Lögren and R. Haas, "Sea level measurements using multi-frequency GPS and GLONASS observations," *EURASIP J. Adv. Signal Process.*, vol. 2014, no. 1, pp. 1–13, Dec. 2014.

[18] W. Liu *et al.*, "Coastal sea-level measurements based on GNSS-R phase altimetry: A case study at the Onsala space observatory, Sweden," *IEEE Trans. Geosci. Remote Sens.*, vol. 55, no. 10, pp. 5625–5636, Oct. 2017.

[19] F. Fabra, "Phase altimetry with dual polarization GNSS-R over sea ice," *IEEE Trans. Geosci. Remote Sens.*, vol. 50, no. 6, pp. 2112–2121, Jun. 2011.

[20] A. M. Semmling *et al.*, "Sea surface topography retrieved from GNSS reflectometry phase data of the GEOHALO flight mission," *Geophys. Res. Lett.*, vol. 41, no. 3, pp. 954–960, 2014.

[21] L. Liou, J. Tsui, D. Lin, J. Schamus, F. Van Graas, and Y. Morton, "Passive altimeter study using GPS flight data," in *Proc. 16th Int. Tech. Meeting Satell. Division The Inst. Navigat. (ION GPS/GNSS)*, 2003, pp. 1264–1270.

[22] H. Carreno-Luengo and A. Camps, "First dual-band multiconstellation GNSS-R scatterometry experiment over boreal forests from a stratospheric balloon," *IEEE J. Sel. Topics Appl. Earth Observ. Remote Sens.*, vol. 9, no. 10, pp. 4743–4751, Oct. 2016.

[23] H. Carreno-Luengo, "Contributions to GNSS-R Earth remote sensing from nano-satellites," Ph.D. dissertation, Dept. Aerosp. Sci. Technol., Universitat Politécnica de Catalunya, Barcelona, Spain, 2016.

[24] A. M. Semmling, V. Leister, J. Saynisch, F. Zus, S. Heise, and J. Wickert, "A phase-altimetric simulator: Studying the sensitivity of Earth-reflected GNSS signals to ocean topography," *IEEE Trans. Geosci. Remote Sens.*, vol. 54, no. 11, pp. 6791–6802, Nov. 2016.

[25] W. Li, E. Cardellach, F. Fabra, A. Rius, S. Ribó, and M. Martín-Neira, "First spaceborne phase altimetry over sea ice using TechDemoSat-1 GNSS-R signals," *Geophys. Res. Lett.*, vol. 44, pp. 8369–8376, Aug. 2017.

[26] W. Li, E. Cardellach, F. Fabra, S. Ribó, and A. Rius, "Lake level and surface topography measured with spaceborne GNSS-reflectometry from CYGNSS mission: Example for the lake Qinghai," *Geophys. Res. Lett.*, vol. 45, no. 24, pp. 13–332, Dec. 2018.

[27] Y. Wang and Y. J. Morton, "Coherent and semi-coherent spaceborne GNSS-R for land surface altimetry applications," in *Proc. 33rd Int. Tech. Meeting Satell. Division Inst. Navigat. (ION GNSS)*, Oct. 2020, pp. 3901–3908.

[28] S. Gleason, "Remote sensing of ocean, ice and land surfaces using bistatically scattered GNSS signals from low Earth orbit," Ph.D. dissertation, Dept. Appl. Phys., Univ. Surrey, Guildford, U.K., 2006.

[29] C. Roesler, Y. Wang, Y. J. Morton, and R. S. Nerem, "Coherent GPS reflections over ocean surface," in *Proc. IEEE Int. Geosci. Remote Sens. Symp. (IGARSS)*, Oct. 2020, pp. 6218–6221.

[30] V. Irisov, T. Duly, V. Nguyen, and D. Masters, "Radio occultation atmospheric profiling from the Spire nanosatellite constellation and its impact on weather forecasting," *Proc. SPIE*, vol. 11531, Sep. 2020, Art. no. 115310G.

[31] V. Nguyen, J. Cartwright, O. Nogues-Correig, T. Yuasa, V. Irisov, and D. Masters, "Sea ice altimetry and classification using grazing angle reflected GNSS signals measured by Spire's nanosatellite constellation," in *Proc. AGU Fall Meeting Abstr.*, 2020, p. 0014.

[32] Y. Wang, Y. Liu, C. Roesler, and Y. J. Morton, "Detection of coherent GNSS-R measurements using a support vector machine," in *Proc. IEEE Int. Geosci. Remote Sens. Symp. (IGARSS)*, Oct. 2020, pp. 6210–6213.

[33] V. A. Nguyen, O. Nogués-Correig, T. Yuasa, D. Masters, and V. Irisov, "Initial GNSS phase altimetry measurements from the spire satellite constellation," *Geophys. Res. Lett.*, vol. 47, no. 15, Aug. 2020, Art. no. e2020GL088308.

[34] U. Inan and A. Inan, *Reflection, Transmission, and Refraction of Waves at Planar Interfaces*. Upper Saddle River, NJ, USA: Prentice-Hall, 2000.

[35] F. T. Ulaby, R. K. Moore, and A. K. Fung, *Microwave Remote Sensing: Active and Passive. From, Theory to Applications*. Norwood, MA, USA: Artech House. 1986.

[36] F. F. Cervellera, "GNSS-R as a source of opportunity for remote sensing of the cryosphere," Ph.D. dissertation, Dept. Signal Theory Commun., Universitat Politécnica de Catalunya, Barcelona, Spain, 2013.

[37] F. Martin *et al.*, "Mitigation of direct signal cross-talk and study of the coherent component in GNSS-R," *IEEE Geosci. Remote Sens. Lett.*, vol. 12, no. 2, pp. 279–283, Feb. 2014.

[38] J. F. Munoz-Martin *et al.*, "Untangling the incoherent and coherent scattering components in GNSS-R and novel applications," *Remote Sens.*, vol. 12, no. 7, p. 1208, Apr. 2020.

[39] E. Loria, A. O'Brien, and I. J. Gupta, "Detection & separation of coherent reflections in GNSS-R measurements using CYGNSS data," in *Proc. IEEE Int. Geosci. Remote Sens. Symp. (IGARSS)*, Jul. 2018, pp. 3995–3998.

[40] I. M. Russo, M. di Bisceglie, C. Galdi, M. Lavalle, and C. Zuffada, "Wave coherence in GNSS reflectometry: A signal processing point of view," in *Proc. IEEE Int. Geosci. Remote Sens. Symp. (IGARSS)*, Sep. 2020, pp. 6214–6217.

[41] M. M. Al-Khaldi, J. T. Johnson, S. Gleason, E. Loria, A. J. O'Brien, and Y. Yi, "An algorithm for detecting coherence in cyclone global navigation satellite system mission level-1 delay-Doppler maps," *IEEE Trans. Geosci. Remote Sens.*, vol. 59, no. 5, pp. 4454–4463, May 2020.

[42] M. Al-Khaldi *et al.*, "Intercomparisons of coherence detectors," in *Proc. CYGNSS Sci. Team Meeting*, Apr. 2020.

[43] H. Kramer. (2020). *Lemur-2 Nanosatellite Constellation of Spire Global*. eoPortal Directory. [Online]. Available: https://directory.eoportal.org/web/eoportal/satellite-missions/l/lemur

[44] D. Masters, V. Nguyen, I. Vladimir, and T. Duly, "User documentation: Spire radio occultation processing and file formats," Version 1.3, Spire Global Inc., Vienna, VA, USA, 2019.

[45] F. Fetterer, K. Knowles, W. N. Meier, M. Savoie, and A. K. Windnagel, "Sea ice index, version 3, updated daily," Nat. Snow Ice Data Center, Boulder, CO, USA, 2017. Accessed: Jul. 10, 2021, doi: 10.7265/N5K072F8.

[46] M. Katzin, "The scattering of electromagnetic waves from rough surfaces," *Proc. IEEE*, vol. 52, no. 11, pp. 1389–1390, Mar. 1964.

[47] J.-C. Kucwaj, S. Reboul, G. Stienne, J.-B. Choquel, and M. Benjelloun, "Circular regression applied to GNSS-R phase altimetry," *Remote Sens.*, vol. 9, no. 7, p. 651, 2017.

[48] N. I. Fisher, *Statistical Analysis of Circular Data*. Cambridge, U.K.: Cambridge Univ. Press, 1995.

[49] J. Cai, E. W. Grafarend, and C. Hu, "The statistical property of the GNSS carrier phase observations and its effects on the Hy-pothesis testing of the related estimators," in *Proc. 20th Int. Tech. Meeting Satell. Division The Inst. Navigat. (ION GNSS)*, 2007, pp. 331–338.

[50] B. Breitsch, Y. T. Morton, C. Rino, and D. Xu, "GNSS carrier phase cycle slips due to diffractive ionosphere scintillation: Simulation and characterization," *IEEE Trans. Aerosp. Electron. Syst.*, vol. 56, no. 5, pp. 3632–3644, Oct. 2020.

[51] J. Mashburn, P. Axelrad, C. Zuffada, E. Loria, A. O'Brien, and B. Haines, "Improved GNSS-R ocean surface altimetry with CYGNSS in the seas of Indonesia," *IEEE Trans. Geosci. Remote Sens.*, vol. 58, no. 9, pp. 6071–6087, Sep. 2020.

[52] ERA5. (2020). *Fifth Generation ECMWF Reanalysis for the Global Climate*. [Online]. Available: https://cds.climate.copernicus.eu/cdsapp#!/home

[53] H. Hersbach *et al.*, "The ERA5 global reanalysis," *Quart. J. Royal Meteorolog. Soc.*, vol. 146, no. 730, pp. 1999–2049, 2020.

[54] M. Tschudi, W. N. Meier, J. S. Stewart, C. Fowler, and J. Maslanik, "EASE-grid sea ice age, version 4," Nat. Snow Ice Data Center, Boulder, CO, USA, 2019. Accessed: Jul. 10, 2021, doi: 10.5067/UTAV7490FEPB.

[55] M. B. Rivas, J. A. Maslanik, and P. Axelrad, "Bistatic scattering of GPS signals off Arctic sea ice," *IEEE Trans. Geosci. Remote Sens.*, vol. 48, no. 3, pp. 1548–1553, Mar. 2009.

[56] N. Rodriguez-Alvarez, B. Holt, S. Jaruwatanadilok, E. Podest, and K. C. Cavanaugh, "An Arctic sea ice multi-step classification based on GNSS-R data from the TDS-1 mission," *Remote Sens. Environ.*, vol. 230, Sep. 2019, Art. no. 111202.

[57] UCAR. (2019). *GPS Data Bits Hourly Archive Files*. [Online]. Available: https://cosmic-io.cosmic.ucar.edu/cdaac/login/fidrt/level1a/bitArc/

[58] Y. Wang, B. Breitsch, and Y. T. J. Morton, "A state-based method to simultaneously reduce cycle slips and noise in coherent GNSS-R phase measurements from open-loop tracking," *IEEE Trans. Geosci. Remote Sens.*, vol. 59, no. 10, pp. 8873–8884, Oct. 2021, doi: 10.1109/TGRS.2020.3036031.

[59] O. Andersen, P. Knudsen, and L. Stenseng, "A new DTU18 MSS mean sea surface—Improvement from SAR altimetry," in *Proc. 25 Years Prog. Radar Altimetry Symp.*, 2018.

[60] G. D. Egbert and S. Y. Erofeeva, "Efficient inverse modeling of barotropic ocean tides," *J. Atmos. Ocean. Technol.*, vol. 19, pp. 183–204, Feb. 2002.

[61] S.-C. Wu, T. Meehan, and L. Young. (1997). *The Potential Use of GPS Signals as Ocean Altimetry Observables*. JPL. [Online]. Available: https://hdl.handle.net/2014/21658

[62] D. Landskron and J. Böhm, "VMF3/GPT3: Refined discrete and empirical troposphere mapping functions," *J. Geodesy*, vol. 92, no. 4, pp. 349–360, Apr. 2018.

**Carolyn J. Roesler** received the Ph.D. degree in aerospace engineering from the University of Colorado Boulder, Boulder, CO, USA, in 2014, with a focus on coastal altimetry.

She is currently an Associate Research Assistant with the Satellite Navigation and Sensing (SeNSe) Laboratory, University of Colorado Boulder. Her research interests lie in Global Navigation Satellite System (GNSS) reflectometry applications for land and ocean remote sensing.

**Y. Jade Morton** (Fellow, IEEE) received the Ph.D. degree in electrical engineering (EE) from Penn State, State College, PA, USA, in 1991.

She was an EE Professor with Colorado State University, Fort Collins, CO, USA, and Miami University, Oxford, OH, USA, prior to joining the University of Colorado Boulder (CU), Boulder, CO, USA, in 2017. She is currently the Helen and Hubert Croft Professor of Engineering, the Director of the Colorado Center for Astrodynamics Research (CCAR), and the Head of the Satellite Navigation and Sensing (SeNSe) Laboratory, Ann and H. J. Smead Department of Aerospace Engineering Sciences, CU. Her research interests lie at the intersection of satellite navigation technologies and remote sensing of the Earth's space environment, atmosphere, and surface.

Dr. Morton is also a fellow of the Institute of Navigation (ION) and the Royal Institute of Navigation (RIN). She is an Institute of Navigation (ION) Thurlow, Burka and Kepler Award Winner and an IEEE Kershner Award Winner. She is also a Distinguished Lecturer.

**Yang Wang** (Student Member, IEEE) received the B.E. degree from Beihang University, Beijing, China, in 2013, and the M.E. degree from Nanyang Technological University (NTU), Singapore, in 2016. He is currently pursuing the Ph.D. degree in aerospace engineering sciences with the University of Colorado Boulder, Boulder, CO, USA.

His research focuses on Global Navigation Satellite System (GNSS) signal processing and remote sensing applications.

**R. Steven Nerem** received the Ph.D. degree in aerospace engineering from The University of Texas at Austin, Austin, TX, USA, in 1989.

He is currently a Professor of aerospace engineering sciences with the University of Colorado Boulder (CU), Boulder, CO, USA, where he is also an Associate Director of the Colorado Center for Astrodynamics Research and a fellow of the Cooperative Institute for Research in Environmental Sciences. He is a specialist in satellite remote sensing and geodesy, with the main research focus on measuring sea-level change using satellite altimetry and satellite gravity data. He pioneered the use of satellite altimetry for measuring long-term sea-level change related to climate variations and determining the causes of the observed changes. He was a Lead Author of the IPCC 5th Assessment Report and has participated in several NASA satellite flight projects, including TOPEX/Poseidon, Jason-1, GRACE, and Jason-2.

Dr. Nerem was elected as a fellow of the American Geophysical Union in 2008.